Paper

REVISIONS TO THE ORNL SERIES OF ADULT AND PEDIATRIC COMPUTATIONAL PHANTOMS FOR USE WITH THE MIRD SCHEMA

Eun Young Han,* Wesley E. Bolch,*† and Keith F. Eckerman‡

Abstract—**The age-dependent series of stylized computational phantoms developed at the Oak Ridge National Laboratory in the late 1970's to early 1980's has found wide applicability in dosimetry studies ranging from dose coefficient compilations for external and internal photon emitters, simulations of patient radiological exams, and dose reconstruction activities. In the present study, we report on a series of revisions to the Oak Ridge National Laboratory series for their intended use within the MIRD schema of medical internal dosimetry. These revisions were made to (1) incorporate recent developments in stylized models of the head, brain, kidneys, rectosigmoid colon, and extra-pulmonary airways; (2) incorporate new models of the salivary glands and the mucosa layer of the urinary bladder, alimentary tract organs, and respiratory airways; (3) adopt reference values of elemental tissue compositions and mass densities from ICRP Publication 89 and ICRU Report 46; (4) provide for explicit treatment of left and right organs within organ pairs; (5) provide for a systematic tabulation of electron absorbed fractions as a function of energy and subject age for all internal organs; and (6) provide for methods of deriving patient-specific values of the specific absorbed fraction for both electrons and photons through interpolation/extrapolation of their phantom-derived values. While tomographic computational phantoms provide improved anatomic realism given the CT or MR image sets used in their construction, there does not yet exist a comprehensive series of reference pediatric tomographic phantoms, nor the ability to simulate very fine anatomic structures as can be modeled via mathematical approximation. Consequently, stylized pediatric phantoms will continue to fill this data need in medical dosimetry.**

Health Phys. 90(4):337–356; 2006

Key words: dose, internal; modeling, dose assessment; Monte Carlo; nuclear medicine

INTRODUCTION

THE SERIES of stylized (or mathematical) computational phantoms developed at the Oak Ridge National Laboratory (ORNL) in the early 1980's have been used extensively in the study of organ doses in nuclear medicine (Stabin and Sparks 2003; Stabin 1996), projection radiography (Jones and Wall 1985; Rosenstein 1988; Staton et al. 2003), diagnostic and interventional fluoroscopy (Bolch et al. 2003; Stern et al. 1995; Suleiman et al. 1991), environmental radiation exposures (Eckerman et al. 1999; Eckerman and Ryman 1993), and radiation protection (ICRP 1989, 1993, 1994, 1995a, 1995b, 2001). These phantoms utilize 3D surface equations to represent both internal organ structure and external body shape. The ORNL series are hermaphrodites (inclusive of both male and female organs and tissues), and include mathematical representations of a newborn, 1-y-old, 5-y-old, 10-y-old, 15-y-old, and an adult male. The 15-y model was originally considered to be representative of the adult female until the publication of ORNL/TM-12907 (Stabin et al. 1995) in which photon specific absorbed fractions from the 15-y phantom were rescaled to explicitly match adult female ICRP reference masses. In their original design, adult organ volumes (defined by their mathematical surface equations) were set so that their product with reference tissue densities provided reasonable agreement with reference organ masses given in ICRP Publication 23 (ICRP 1975). Reference organ masses for the younger phantoms were not given in ICRP Publication 23, and thus other literature sources were consulted during model construction (Cristy 1980). For all phantoms except the newborn, three tissue compositions were assumed—soft tissue (1.04 g cm^{-3}), homogeneous skeleton (bone and marrow at 1.4 g cm^{-3}), and homogeneous lung (soft tissue and air at 0.296 g cm^{-3}). A slightly different elemental composition was adopted for the newborn soft tissues (1.04 g cm^{-3}) and the newborn skeleton (1.22 g cm^{-3}).

In this study, revisions to the ORNL series of stylized anatomic phantoms are described for their subsequent use

* Department of Nuclear and Radiological Engineering, University of Florida, Gainesville, FL 32611-8300; † Department of Biomedical Engineering, University of Florida, Gainesville, FL 32611-8300; Life Sciences Division, Oak Ridge National Laboratory, Oak Ridge, TN 37830.

For correspondence or reprints contact: Wesley E. Bolch, Advanced Laboratory for Radiation Dosimetry Studies (ALRADS), Department of Nuclear and Radiological Engineering, University of Florida, Gainesville, FL 32611-8300, or email at wbolch@ufl.edu.

(*Manuscript received* 13 *May* 2005; *revised manuscript received* 26 *July* 2005, *accepted* 18 *November* 2005)

0017-9078/06/0

within the MIRD schema (Howell 1994). First, previously published stylized models of the head and brain, the extrathoracic-thoracic airways, the kidneys, and the rectosigmoid colon were incorporated within the mathematical structure of the ORNL model series. Second, new models of the salivary glands and the mucosa layer of the alimentary tract organs, the respiratory tract airways, and the urinary bladder were designed at each phantom age. Third, tissue compositions and mass densities published in ICRP Publication 89 (ICRP 2002) and ICRU Report 46 (ICRU 1992) were adopted. When mathematical adjustments to organ volumes were feasible as constrained by the boundaries of adjacent organs, these changes were made in order to bring revised organ masses to within $\pm 10\%$ of their age-dependent ICRP 89 values. The revised ORNL series was then incorporated within the input structure of the MCNP5 Monte Carlo radiation transport code for simulation of both internal photon and electron sources. In consultation with the Society of Nuclear Medicine's MIRD committee, photon and electron specific absorbed fractions are scheduled to be published in monograph form in 2006.

A second type of anatomic phantom that exists for use in radiation protection are tomographic or voxel-based computational phantoms constructed from segmented CT or MR images of a single individual. In the near future, the International Commission on Radiological Protection (ICRP) will formally adopt new adult male and female tomographic voxel-based computational phantoms for its upcoming radiation protection recommendations. While improved anatomic realism is clearly evident in such phantoms, many of the finer anatomic features needed for dose assessment can be problematic as input CT or MR images are available at resolutions of several millimeters—dimensions far larger than some ICRP-defined target tissues (e.g., tens of μm). In these cases, the stylized anatomic phantoms are needed to supplement radiation transport results from voxel-based phantoms, particularly in regard to absorbed fractions for beta and alpha particles. While a limited number of studies have reported the construction of tomographic computational phantoms of children (Caon et al. 1999; Nipper et al. 2002; Zankl et al. 1988), a complete reference series of pediatric voxel phantoms is not currently available, and thus stylized pediatric phantoms will continue to fill that data need in medical radiation dosimetry.

MATERIALS AND METHODS

Adoption of previously published organ models

Four major modifications were made to the ORNL phantom series in which previously published organ-specific models were incorporated within the overall body structure of the ORNL phantom series. The first revision involved the adoption of the age-dependent MIRD head and brain model as given in MIRD Pamphlet No. 15 and its subsequent monograph (Bouchet et al. 1999a and b). Exceptions included (1) removal of the MIRD-15 brain substructures (ventricles, thalamus, caudate nucleus, etc.) and (2) homogenization of the bone and soft tissue regions of the cervical spine (spinal cord and spinal fluid were not included). Revisions were additionally made to the shape of the spine (cervical, thoracic, lumbar/sacrum sections) as the ORNL spine is more elliptical in cross section than that given in MIRD 15. If more detailed intra-brain sub-region dosimetry is required as in radiopharmaceutical neuroimaging, the model of MIRD Pamphlet No. 15 should be consulted.

Second, the age-dependent multi-region kidney models of MIRD Pamphlet No. 19 were adopted (Bouchet et al. 2003). These models include separate sub-organ models for the renal cortex, medulla, and pelvis within the original boundaries of the ORNL kidney series. Third, revisions suggested by Mardirossian et al. for the rectosigmoid colon and associated re-positioning of the prostate glad and urinary bladder were adopted as published (Mardirossian et al. 1999). Finally, the stylized representations of the extrathoracic airways, trachea, and extra-pulmonary bronchi given by Farfán et al. for the adult model were adopted and rescaled for inclusion in the revised ORNL pediatric phantoms (Farfán et al. 2004).

Salivary glands

Mathematical models of the salivary glands were created for insertion within the oral cavity of the revised ORNL series. The three pairs of ellipsoidal salivary glands were designed with volumes selected to match their ICRP 89 age-dependent tissue masses (ICRP 2002) and with shapes guided by histological photographs and anatomic drawings (Marieb 2001; Netter and Hansen 2003). Fig. 1 shows a frontal view of one of each pair of the salivary glands—the left parotid, the left sublingual, and the left submandibular glands. In their descriptions below, the "$\pm$" sign is taken as positive for the right gland and negative for the left gland. Numerical values for all parameters are given in Table 1.

The parotid glands are modeled as two elliptical cylinders parallel to the z-axis and located in the soft tissue region medial to the lateral sides of the mandible. The defining equations for the parotid glands are given as:

$$\left(\frac{x \pm x_{PG}}{a_{PG}}\right)^2 + \left(\frac{y - y_{PG}}{b_{PG}}\right)^2 \leq 1, \quad (1)$$

$$\text{and } z_{PG1} \leq z \leq z_{PG2}. \quad (2)$$

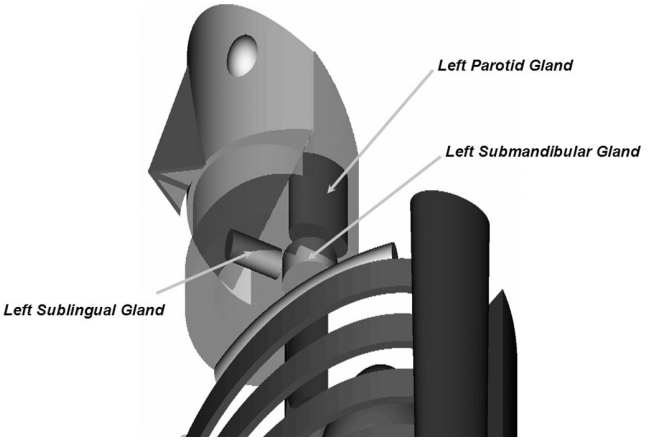

Fig. 1. Frontal view of the left set of salivary glands within the revised ORNL phantom of the adult patient.

The sublingual glands are modeled as two right circular cylinders parallel to the *y*-axis and located in the soft tissue region medial to the anterior portion of the mandible. The defining equations for the sublingual glands are given as:

$$\left(\frac{x \pm x_{\mathrm{LG}}}{r_{\mathrm{LG}}}\right)^2 + \left(\frac{z - z_{\mathrm{LG}}}{r_{\mathrm{LG}}}\right)^2 \leq 1, \tag{3}$$

$$\text{and } y_{\mathrm{LG1}} \leq y \leq y_{\mathrm{LG2}}. \tag{4}$$

The submandibular glands are modeled as two right circular cylinders parallel to the *z*-axis and located in the soft tissue region medial to the posterior portion of the mandible. The defining equations for the submandibular glands are given as:

$$\left(\frac{x \pm x_{\mathrm{MG}}}{r_{\mathrm{MG}}}\right)^2 + \left(\frac{y - y_{\mathrm{MG}}}{r_{\mathrm{MG}}}\right)^2 \leq 1, \tag{5}$$

$$\text{and } z_{\mathrm{MG1}} \leq z \leq z_{\mathrm{MG2}}. \tag{6}$$

Mucosal layer of the urinary bladder, alimentary tract organs, and respiratory airways

In its present formulation, the MIRD schema assigns the absorbed dose to the walls of the urinary bladder and alimentary tract organs as averaged over the entire wall thickness, while the absorbed dose from particulate radiations (e.g., beta particles) is assigned as a point dose estimate at the wall-content interface. Anatomically, different tissue sublayers exist for the urinary bladder (mucosa, muscularis externa, and adventitia) and alimentary tract organs (mucosa, submucosa, muscularis externa, and serosa), with the mucosa layer housing, at various depths, those cell populations responsible for both chronic and acute radiation injury. In the present study, the walls of these organs in the ORNL series are partitioned into a mucosa layer and a residual wall layer through the use of mean ratios of mucosa-to-total wall thickness. In Table 2, mucosa thicknesses are given for the esophagus, stomach, small intestine, large intestine, and urinary bladder as expressed as a fraction of their total wall thickness. Data sources include both microphotographic slides of wall histology, as well as direct measurements from endoscopic ultrasound (Huh et al. 2003). Coefficients of variation on the mucosal thickness ratio are listed at the bottom of Table 2 and represent to a large extent the biological variability as might be seen in the general population. Values of COV range from 16% for the small intestine ($n = 3$) to 36% for the urinary bladder ($n = 7$). In the present study, monoenergetic photons or electron sources are taken to be either uniformly localized within the lumen contents, or are uniformly localized within the mucosa layer itself. The target region for compilation of both photon and electron absorbed fractions under the MIRD schema is the mucosa layer in each of these organs. In Table 3, similar data are given for the fractional wall thicknesses of the mucosal layers of the larynx, trachea, and main bronchi. The fractional wall thickness of the pharynx mucosa is taken to be that for the larynx mucosa.

Elemental compositions and tissue densities

In Section 13 of ICRP Publication 89, reference elemental compositions are given for all major organs and tissues in the adult, children, and newborn. As indicated in Table 4, we have adopted these elemental compositions within the revised ORNL model series. These elemental compositions, in many cases, correspond to those given in Appendix A of ICRU Report 46, and thus the corresponding tissue mass densities from ICRU 46 were adopted as well. For example, the elemental composition of the adult/child liver in ICRP 89 matches that given in ICRU 46 for "adult–fatty" liver for which a tissue density of 1.05 g cm^{-3} is reported. Correspondingly, the reference elemental composition for the newborn liver in ICRP 89 corresponds to that for the 1-y-old child in ICRU 46, also at a density of 1.05 g cm^{-3}. As another example, the ICRU reference elemental composition of adult/child breast tissue corresponds to that in ICRU Report 46 for a 33–67% glandular/lipid tissue mixture at a density of 0.94 g cm^{-3}.

Independent consideration of left and right organs within organ pairs

In some instances, radiopharmaceutical uptake may differ between the right and left organs within organ pairs due to metabolic failure or vasculature injury. Traditional compilations of photon specific absorbed fractions, however, have considered the photon source to be distributed

Table 1. Ellipsoidal parameters used to define the age-dependent salivary gland volumes within the revised ORNL anatomic series.

Parameter	Newborn	1-y	5-y	10-y	15-y	Adult
Salivary glands—Parotid						
a_{PG}	0.254	0.3815	0.5681	0.563	0.9127	1.063
b_{PG}	1.24	1.6	1.82	1.89	1.9	2
x_{PG}	1.15	1.6	1.75	1.825	1.875	2.5
y_{PG}	−1.24	−1.605	−1.82	−1.895	−1.905	−2.025
z_{PG1}	25.10	35.29	46.24	56.76	69.97	77.4
z_{PG2}	26.8	38.8	49.2	60.5	73.5	81
Salivary glands—Sublingual						
r_{LG}	0.220	0.398	0.44	0.48	0.601	0.666
x_{LG}	0.32	0.5	0.54	0.58	0.7	0.8
y_{LG1}	−4.7	−3.2	−3.64	−7.1	−3.81	−4.05
y_{LG2}	−2.49	−6.1	−6.8	−3.79	−7.2	−7.5
z_{LG}	24.88	34.892	45.8	56.279	69.369	76.734
Salivary glands—Submandibular						
r_{MG}	0.517	0.813	0.99	1.247	1.495	1.761
x_{MG}	1.05	1.6	1.6	1.7	1.75	1.8
y_{MG}	−1.963	−2.407	−2.64	−2.533	−0.230	−2.3
z_{MG1}	23.85	33.27	44.24	55.0	68.0	75.5
z_{MG2}	24.88	34.892	45.8	56.279	69.369	76.734

Table 2. Mucosa thicknesses for the alimentary tract organs and urinary bladder expressed as a fraction of the total wall thickness. Average values for each organ were adopted within the stylized model series. These ratios were assumed to be independent of subject age.

Organs	Esophagus	Stomach	Small intestine	Large intestine	Urinary bladder
	0.38[a]	0.30[d,f]	0.47[b]	0.35[b]	0.16[b]
	0.25[b]	0.42[e]	0.42[d]	0.33[m]	0.10[e]
	0.14[c]	0.32[k]	0.57[e]	0.36[d]	0.27[f]
	0.16[d]	0.48[g]		0.26[e]	0.25[g]
	0.25[e]	0.35[l]		0.29[f]	0.16[i]
	0.27[f]	0.42[j]		0.18[g]	0.18[j]
	0.30[g]			0.25[i]	0.12[o]
	0.21[h]			0.16[n]	
	0.27[i]			0.26[j]	
	0.25[j]			0.32[k]	
				0.27[j]	
Average ratio	0.25	0.38	0.49	0.28	0.18
COV (%)	27%	18%	16%	23%	36%

[a] Weiss (1984).
[b] di Fiore and Schmidt (1981).
[c] Marieb (2001).
[d] Ross et al. (1995).
[e] Zhang (1999).
[f] Tortora and Anagnostakos (1984).
[g] Reith and Ross (1965).
[h] Ross et al. (2002).
[i] Herrath (1966).
[j] di Fiore and Eroschenko (1989).
[k] Huh et al. (2003).
[l] Gartner and Hiatt (1987).
[m] Sleisenger et al. (1998).
[n] Kerr (1999).
[o] Bergman et al. (1989).

uniformly within both the right or left tissues of paired organs. In the current study, left and right organs are considered independently as source regions for both photon and electron emissions. These pairs include the lungs (source and target), the kidneys and their subregions (source and target), the adrenal glands (source and target), the breasts (source and target), and the eyes (target).

Table 3. Mucosa thicknesses for the respiratory tract airways expressed as a fraction of the total wall thickness. Average values for each organ are adopted within the stylized model series and are assumed to be independent of subject age.

Organs	Larynx	Pharynx	Trachea	Main bronchi
	0.39[a]		0.22[a] 0.11[b] 0.15[c] 0.25[d] 0.29[e]	0.25[b] 0.17[c] 0.27[f]
Average ratio	0.39	0.39	0.20	0.23
COV (%)			37%	23%

[a] Eroschenko and di Fiore (2000).
[b] Berman (2003).
[c] Junqueira and Carneiro (2003).
[d] Zhang (1999).
[e] Burkitt et al. (1993).
[f] Junqueira and Carneiro (2003).

Adjustments to original organ volumes

With the publication of new reference organ masses in ICRP Publication 89, selected revisions to organ volumes in the original ORNL series were attempted as feasible. In those cases where a mass difference exists between the ORNL organ mass and the ICRP 89 organ mass, a change in organ volume was attempted noting slight changes as well in ICRU tissue densities from the 3-tissue composition in the original ORNL series. Volume decreases were easily accommodated, while volume increases were constrained by the need to avoid organ boundary overlap within the rigid structure of the mathematical phantom series. For new organs such as the larynx and pharynx walls, a decision was made to preserve the reference wall thickness (for electron transport simulations), and to then match reference organ masses as best as possible using only the length of the organ in the +z and –z directions. For sections of the large colon, wall thicknesses in the original ORNL series were set artificially high in order to match ICRP 23 reference wall masses given that reference colon lengths could not be accommodated within the stylized abdomen. For similar reasons, these wall thicknesses and sectional lengths were retained in the revised phantom series.

For the adult model, organ volumes were increased for the pancreas (+29%), breasts (+40%), thymus (+23%), and ovaries (+20%), while decreases in organ volumes were made for the adrenal glands (−14%) and spleen (−18%). For the 15-y model, organ volumes were increased for the pancreas (+59%), breast tissue (+36%), and thymus (+20%), while decreases in organ volumes were made for the esophageal wall (−7%) and gallbladder wall (−15%). As this model represents both the adult female as well as 15-y-old hermaphrodite, compromises in the selection of the target organ mass had to be made (discussed later in this paper). The ICRP reference 15-y-old female has only recently been defined within ICRP Publication 89, and no attempt was made to accommodate her within the redesign of the ORNL 15-y model.

For the 10-y model, organ volumes were increased for the pancreas (+80%) and thymus (+26%), while decreases in organ volumes were made for the gallbladder wall (−38%) and contents (−33%). For the 5-y model, organ volumes were increased for the pancreas (+39%), while decreases in organ volumes were made for the gallbladder wall (−22%) and its contents (−20%). For the 1-y model, organ volumes were increased for the gallbladder wall (+51%) and its contents (+53%), pancreas (+81%), thymus (+20%), and testes (+13%). Finally, organ volumes in the newborn model were increased for the gallbladder wall (+17%) and its contents (+19%), the pancreas (+93%), and the urinary bladder wall (+24%).

The tissue density of the lungs given in both ICRU Report 46 and ICRP Publication 89 is 0.26 g cm^{-3} and represents an effective density for the homogenized lung (tissue parenchyma, pulmonary blood, and airway contents). This value is lower than the value of 0.296 g cm^{-3} adopted in the original ORNL phantom series, and was found to provide inconsistent matching between original ORNL lung volumes and ICRP 89 reference lung masses (inclusive of their blood content). Attempts were made to adjust lung volumes in the ORNL series using this lower recommended effective density, but this effort proved difficult as many of the lung volumes had to be expanded beyond that permitted by the fixed geometries of the rib cage and heart. Consequently, one of two options were available: (1) assign a unique effective lung density to each phantom to force agreement with ICRP 89 reference masses, or (2) optimize the assignment of a single effective

Table 4. Reference of elemental compositions and mass densities adopted in this study.

	Adult, 15 y, 10 y, 5 y, and 1 y models		Newborn model	
Organ/Tissue	Elemental composition (ICRU 46/ICRP 89)	Mass density (g cm^{-3}) (ICRU 46)	Elemental composition (ICRU 46/ICRP 89)	Mass density (g cm^{-3}) (ICRU 46)
Respiratory system				
External nose	ICRU 46—Skeletal muscle (adult)	1.05	ICRU 46—Skeletal muscle (newborn)	1.05
Oral cavity	ICRU 46—Average soft tissue (male)	1.03	ICRU 46—Average soft tissue (male)	1.02 (ORNL—NB SG)
Larynx	ICRP 89—Table 13.2	1.10 (cartilage)	ICRP 89—Table 13.5	1.10 (cartilage)
Pharynx	ICRU 46—Skeletal muscle (adult)	1.05	ICRU 46—Skeletal muscle (newborn)	1.05
Trachea	ICRP 89—Table 13.2	1.03 (soft tissue—M)	ICRP 89—Table 13.5	1.02 (ORNL—NB SG)
Main bronchi	ICRU 46—Average soft tissue (male)	1.03	ICRU 46—Average soft tissue (male)	1.03
Lungs	ICRP 89—Table 13.2	0.352 (effective)	ICRP 89—Table 13.5	0.352 (effective)
Respiratory airways	Air	0.001205	Air	0.001205
Alimentary system				
Salivary glands	ICRU 46—Average soft tissue (male)	1.03	ICRU 46—Average soft tissue (male)	1.03
Esophagus wall	ICRP 89—Table 13.2	1.03 (soft tissue)	ICRP 89—Table 13.5	1.02 (ORNL—NB SG)
Esophagus lumen	Air	0.001205	Air	0.001205
Stomach	ICRP 89—Table 13.2	1.03 (soft tissue)	ICRP 89—Table 13.5	1.03 (soft tissue)
Small intestine	ICRP 89—Table 13.2	1.03 (soft tissue)	ICRP 89—Table 13.5	1.03 (soft tissue)
Colon	ICRP 89—Table 13.2	1.03 (soft tissue)	ICRP 89—Table 13.5	1.03 (soft tissue)
Liver	ICRP 89—Table 13.2	1.05 (adult—fatty)	ICRP 89—Table 13.5	1.05 (1-y child)
Gall bladder	ICRP 89—Table 13.2	1.03 (soft tissue)	ICRP 89—Table 13.5	1.02 (soft tissue)
Pancreas	ICRP 89—Table 13.2	1.04 (adult)	ICRP 89—Table 13.5	1.04 (adult)
ST/Colon contents[a]	ICRU 46—Average soft tissue (male)	1.03	ICRU 46—Average soft tissue (male)	1.03
Circulatory system				
Heart wall	ICRP 89—Table 13.2	1.05 (adult—healthy)	ICRP 89—Table 13.5	1.04 (fetus)
Heart content (blood)	ICRP 89—Table 13.2	1.06 (adult)	ICRP 89—Table 13.5	1.07 (newborn)
Urogenital system				
Kidneys (subregions)	ICRP 89—Table 13.2	1.05 (adult)	ICRP 89—Table 13.5	1.03 (fetus)
Urinary bladder wall	ICRP 89—Table 13.2	1.04 (adult—filled)	ICRP 89—Table 13.5	1.04 (adult—filled)
Urinary bladder cont	ICRP 89—Table 13.2	1.04 (adult—filled)	ICRP 89—Table 13.5	1.04 (adult—filled)
Prostate gland	ICRP 89—Table 13.3	1.03 (soft tissue—M)	ICRP 89—Table 13.6	1.02 (ORNL—NB SG)
Testes	ICRP 89—Table 13.3	1.04 (adult)	ICRP 89—Table 13.6	1.04 (adult)
Genitalia (male)	ICRU 46—Average soft tissue (male)	1.03 (soft tissue—M)	ICRU 46—Average soft tissue (male)	1.02
Ovaries	ICRP 89—Table 13.3	1.05 (adult)	ICRP 89—Table 13.6	1.02 (ORNL—NB SG)
Uterus	ICRP 89—Table 13.3	1.02 (soft tissue—F)	ICRP 89—Table 13.6	1.02 (soft tissue)
Skeletal system				
All bones (less UFR)	ORNL/TM-8381 (1987)	1.40 (homogeneous)	ORNL/TM-8381 (1987)	1.22 (homogeneous)
Upper facial region	50/50 homogeneous bone/soft tissue	1.22 (average density)	50/50 homogeneous bone/soft tissue	1.13 (average density)
Integumentary system				
Skin	ICRP 89—Table 13.2	1.09 (adult)	ICRP 89—Table 13.5	1.05 (newborn)
Additional organs				
Adrenal glands	ICRP 89—Table 13.2	1.03 (soft tissue—M)	ICRP 89—Table 13.5	1.02 (ORNL—NB SG)
Brain	ICRP 89—Table 13.2	1.04 (adult)	ICRP 89—Table 13.5	1.03 (newborn)
Breast tissue	ICRP 89—Table 13.3	0.94 (33/67 water/lipid)	ICRP 89—Table 13.6	0.99 (newborn adipose)
Eyes	ICRP 89—Table 13.2	1.07 (adult)	ICRP 89—Table 13.5	1.07 (adult)
Muscle (head, legs)	ICRP 89—Table 13.2	1.05 (adult)	ICRP 89—Table 13.5	1.05 (newborn)
Muscle (trunk)	ICRU 46—Average soft tissue (male)	1.03	ICRU 46—Average soft tissue (male)	1.03
Spleen	ICRP 89—Table 13.2	1.06 (adult)	ICRP 89—Table 13.5	1.04 (fetus)
Thymus	ICRU 46—Average soft tissue (male)	1.03	ICRU 46—Average soft tissue (male)	1.03
Thyroid	ICRP 89—Table 13.2	1.05 (adult)	ICRP 89—Table 13.5	1.05 (adult)

[a] The rectal portion of the lumen of the rectosigmoid colon is assumed to be air-filled.

lung density across the entire age-range of ORNL phantoms. Physiologically, it can be argued that under option 1, effective lung densities in the phantoms should systematically decrease with increasing phantom age as the lung tree more fully develops resulting in a larger fraction of total lung volume occupied by the pulmonary airways. Option 1, however, yielded effective lung densities that varied erratically with phantom age, and thus option 2 was deemed the more appropriate choice. The final value on the effective lung density adopted in this study was 0.352 g cm^{-3}.

A final tabulation of organ volumes, tissue densities, and organ masses in the revised ORNL series is given in Table 5 for the newborn, 1-y-old, and 5-y-old phantoms. Similar data are given in Table 6 for the 10-y-old, 15-y-old, and adult phantoms. At the bottom of each table, total body masses are given (in kg) for the hermaphrodite, the male version of the model (less the breast tissues), and the female version of the model (less male genitalia and enclosed testes). These hermaphrodite values are 3.52 kg, 9.74 kg, 19.59 kg, 33.11 kg, 57.62 kg, and 75.51 kg for the newborn, 1-y-old, 5-y-old, 10-y-old, 15-y-old, and adult phantoms, respectively. Corresponding values for the original ORNL series are 3.6 kg, 9.7 kg, 19.8 kg, 33.2 kg, 56.8 kg, and 73.7 kg, respectively.

Radiation transport simulations

The entire model series was subsequently encoded within the input structure of the radiation transport code MCNP5 (Briesmeister 1997). For photon sources, particle histories between 8 and 25 million were followed yielding photon-absorbed fractions with coefficients of variation generally less then 5–10% for a majority of source-target organ combinations. As expected, COVs increase with decreasing photon energy, decreasing target organ volume, and increasing source-target organ separation. Coefficients of variation were typically greater than 10% (maximum of ~20%) if the absorbed fraction of photon energy was below 10^{-6}. Photon simulations were made under the kerma approximation, without secondary electron transport.

For electron sources, particle histories between 3 and 5 million were followed at most energies above 100 keV. At lower energies, 10 million electron histories were simulated for improvements in statistical precision. This number of histories was shown to be sufficient to ensure that the electron absorbed fraction for self-organ and adjacent organ irradiation had COVs less then 10%. For all electron simulations, the ITS energy indexing scheme was used in lieu of the default electron transport model in MCNP (Chibani and Li 2002).

RESULTS AND DISCUSSION

Comparisons to ICRP 89 reference organ and total body masses

Table 7 displays ICRP 89 reference organ masses for the newborn, 1-y-old, 5-y-old, and 10-y-old along with their corresponding organ masses in both the original and revised ORNL phantom series. Percent differences between phantom and ICRP 89 reference masses are given for each organ and for both sets of phantoms. Values for "rest of body" under columns labeled "ICRP 89" are derived quantities from data given in Section 13 of ICRP 89, and are defined as the summed masses of (1) separable adipose tissue, (2) skeletal muscle, (3) extra-organ blood volumes, and (4) connective and lymphatic tissues. The mass of blood within the "rest of body" was estimated as 45.1% of the total reference blood mass given in ICRP 89 Table 2.8. Section 7.7.2 of ICRP 89 indicates that the summed blood content of fat, skeletal muscle, lymph nodes, "all other tissues," aorta, and large arteries is ~45.1% in both the adult male and female, and this percentage was assumed to remain constant with age. Estimates of connective and lymphatic tissues were taken to be 4% of the total body mass as per the footnote on Table 2.8 of ICRP 89.

Boxed data in Tables 7 and 8 indicate those organs and phantoms where percent differences between phantom and reference organ masses have either decreased (bolded values) or increased (bold-italicized values) more than 10% as a result of changes in organ volume and/or tissue density. A review of lung masses in both the original and revised ORNL series shows significant improvements in matching ICRP 89 reference lung masses for the newborn (−16% to 0%), the 15-y-old phantom (−28% to −13% for the 15-y-old male and −31% to −17% for the adult female), and the adult phantom (−17% to 0%). However, the use of an age-independent increase in effective lung density from 0.296 to 0.352 g cm^{-3} shows no net improvement in the matching of the reference lung mass in the 10-y-old phantom (−9% to 9%), and slightly worse matching of reference lung masses for the 1-y-old (−5% to 14%) and 5-y-old (−3% to 15%) revised ORNL phantoms.

For the newborn phantom, improvements in reference organ matching are noted for the gall bladder (−23% to −11%), pancreas (−53% to −10%), urinary bladder wall (−29% to −10%), and rest of body (13% to −1%). For the 1-y-old phantom, improvements are noted for the gall bladder (−39% to −8%), pancreas (−49% to −7%), testes (−19% to −9%), and the thymus (−24% to −9%), while an increased discrepancy is seen in total skeletal mass (−3% to 17%). For the 5-y-old and 10-y-old phantoms, improved organ mass matching is

noted for the gall bladder (33% to 5% and 51% to −1%, respectively) and the pancreas (−33% to −6% and −50% to −10%, respectively). In addition, an improvement in reference mass matching is noted for the thymus in the 10-y-old phantom (−16% to 4%).

For the two older phantoms listed in Table 8 (15-y and adult), improvements in organ masses are noted for the pancreas (ICRP 89 15-y-old male and adult male and female), adrenal glands (ICRP 89 adult male), breast tissue (ICRP 89 adult female), spleen (ICRP 89 adult male), and thymus (ICRP 89 15-y and adult males). A significant movement away from ICRP 89 reference masses is noted for the thymus in the 15-y-old phantom when compared to the ICRP 89 adult female thymus

Table 5. Organ and tissue masses in the revised ORNL anatomic models of the newborn, 1-y-old, and 5-y-old.

	Newborn model			1-y model			5-y model		
Organ/Tissue	Volume (cm^3)	Density (g cm^{-3})	Mass (g)	Volume (cm^3)	Density (g cm^{-3})	Mass (g)	Volume (cm^3)	Density (g cm^{-3})	Mass (g)
Respiratory system									
External nose	0.593	1.05	0.623	2.381	1.05	2.500	4.324	1.05	4.540
Nasal cavity (see UFR—Skeleton)									
Sphenoid sinuses	0.738	0.001205	0.001	1.883	0.001205	0.002	2.576	0.001205	0.003
Ethmoid sinuses	0.564	0.001205	0.001	1.439	0.001205	0.002	1.966	0.001205	0.002
Frontal sinuses	1.453	0.001205	0.002	3.755	0.001205	0.005	5.136	0.001205	0.006
Maxillary sinuses	3.825	0.001205	0.005	13.521	0.001205	0.016	18.448	0.001205	0.022
Oral cavity	66.230	1.02	67.555	205.613	1.03	211.781	215.253	1.03	221.711
Larynx—Lumen	0.339	0.001205	0.0004	0.311	0.001205	0.0004	0.753	0.001205	0.001
Larynx—Mucosa	0.174	1.10	0.191	0.238	1.10	0.262	0.446	1.10	0.491
Larynx—Residual wall	0.341	1.10	0.375	0.522	1.10	0.574	0.958	1.10	1.054
Pharynx—Lumen	2.614	0.001205	0.003	4.103	0.001205	0.005	7.360	0.001205	0.009
Pharynx—Mucosa	0.813	1.05	0.854	1.732	1.05	1.819	2.576	1.05	2.705
Pharynx—Residual wall	1.515	1.05	1.591	3.397	1.05	3.567	5.084	1.05	5.338
Trachea—Lumen	0.654	0.001205	0.001	1.405	0.001205	0.002	3.044	0.001205	0.004
Trachea—Mucosa	0.129	1.02	0.132	0.373	1.03	0.384	0.695	1.03	0.716
Trachea—Residual wall	0.631	1.02	0.644	1.868	1.03	1.924	3.403	1.03	3.505
Main bronchi—Lumen	1.335	0.001205	0.002	3.225	0.001205	0.004	5.270	0.001205	0.006
Main bronchi—Mucosa	0.273	1.02	0.278	0.701	1.03	0.722	1.127	1.03	1.161
Main bronchi—Residual wall	1.173	1.02	1.196	2.858	1.03	2.944	4.737	1.03	4.879
Lung—Left	79.100	0.352	27.843	225.000	0.352	79.200	454.000	0.352	159.808
Lung—Right	91.900	0.352	32.349	259.000	0.352	91.168	526.000	0.352	185.152
Total Volume/Mass:	254.394		133.644	733.325		396.881	1,263.156		591.113
Alimentary system									
Salivary glands—Parotid	3.365	1.02	3.432	13.462	1.03	13.866	19.231	1.03	19.808
Salivary glands—Sublingual	1.731	1.02	1.766	6.731	1.03	6.933	9.615	1.03	9.903
Salivary glands—Submandibular	0.673	1.02	0.686	2.885	1.03	2.972	3.846	1.03	3.961
Esophagus—Content	0.385	0.001205	0.0005	0.952	0.001205	0.001	2.126	0.001205	0.003
Esophagus—Mucosa	0.289	1.02	0.295	0.808	1.03	0.832	1.637	1.03	1.686
Esophagus—Residual wall	1.740	1.02	1.775	4.762	1.03	4.905	9.463	1.03	9.747
Stomach—Content	10.200	1.03	10.506	34.800	1.03	35.844	72.200	1.03	74.366
Stomach—Mucosa	2.118	1.03	2.182	7.217	1.03	7.434	16.193	1.03	16.679
Stomach—Residual wall	4.052	1.03	4.174	13.683	1.03	14.093	31.007	1.03	31.937
Small intestine	50.900	1.03	52.427	132.000	1.03	135.960	265.000	1.03	272.950
Right colon—Content	7.705	1.03	7.936	19.850	1.03	20.446	39.900	1.03	41.097
Right colon—Mucosa	1.785	1.03	1.839	4.736	1.03	4.878	9.347	1.03	9.627
Right colon—Residual wall	5.440	1.03	5.603	14.365	1.03	14.796	28.654	1.03	29.514
Left colon—Content	6.805	1.03	7.009	17.560	1.03	18.087	35.020	1.03	36.071
Left colon—Mucosa	1.702	1.03	1.753	4.505	1.03	4.640	8.955	1.03	9.224
Left colon—Residual wall	5.163	1.03	5.318	13.736	1.03	14.148	27.796	1.03	28.630
Rectosigmoid colon—Content	5.016		2.841	13.075		7.130	25.435		13.780
Rectosigmoid colon—Mucosa	0.846	1.03	0.871	2.085	1.03	2.148	4.233	1.03	4.360
Rectosigmoid colon—Residual wall	2.504	1.03	2.579	6.234	1.03	6.421	12.835	1.03	13.220
Liver	117.000	1.05	122.850	281.000	1.05	295.050	562.000	1.05	590.100
Gall bladder—Contents	2.434	1.02	2.483	7.048	1.03	7.259	15.192	1.03	15.648
Gall bladder—Wall	0.458	1.02	0.467	1.317	1.03	1.357	2.786	1.03	2.870
Pancreas	5.204	1.04	5.412	17.838	1.04	18.552	31.511	1.04	32.771
Total Volume/Mass:	237.515		244.204	620.649		637.750	1,233.982		1,267.951
Circulatory system									
Heart—Contents	35.100	1.07	37.557	69.900	1.06	74.094	129.000	1.06	136.740
Heart—Wall	24.400	1.04	25.376	48.700	1.05	51.135	89.300	1.05	93.765
Total Volume/Mass:	59.500		62.933	118.600		125.229	218.300		230.505

Table 5.—*Continued.*

Organ/Tissue	Newborn model			1-y model			5-y model		
	Volume (cm^3)	Density ($g\ cm^{-3}$)	Mass (g)	Volume (cm^3)	Density ($g\ cm^{-3}$)	Mass (g)	Volume (cm^3)	Density ($g\ cm^{-3}$)	Mass (g)
Urogenital system									
Kidneys—Renal cortex	15.360	1.03	15.821	42.140	1.05	44.247	77.780	1.05	81.669
Kidneys—Renal medulla	5.680	1.03	5.850	15.740	1.05	16.527	28.640	1.05	30.072
Kidneys—Renal pelvis	0.920	1.03	0.948	2.560	1.05	2.688	4.700	1.05	4.935
Urinary bladder—Contents	16.110	1.04	16.754	31.700	1.04	32.968	62.200	1.04	64.688
Urinary bladder—Mucosa	0.589	1.04	0.613	1.208	1.04	1.256	2.335	1.04	2.428
Urinary bladder—Residual wall	2.856	1.04	2.970	6.202	1.04	6.450	11.665	1.04	12.132
Prostate gland	0.817	1.02	0.833	0.905	1.03	0.932	1.204	1.03	1.240
Testes	0.811	1.02	0.827	1.306	1.04	1.358	1.570	1.04	1.633
Genitalia (Male)	4.669	1.02	4.762	10.804	1.03	11.128	21.630	1.03	22.279
Ovaries	0.315	1.02	0.321	0.686	1.05	0.720	1.660	1.05	1.743
Uterus	3.700	1.02	3.774	1.400	1.02	1.428	2.600	1.02	2.652
Total Volume/Mass:	51.827		53.474	114.651		119.703	215.984		225.471
Skeletal system									
Cranium	30.900	1.22	37.698	81.100	1.4	113.540	188.300	1.4	263.620
Upper facial region (less sinuses)	40.120	1.13	45.336	135.001	1.22	164.701	159.274	1.22	194.314
Teeth	5.900	1.22	7.198	16.100	1.4	22.540	22.100	1.4	30.940
Mandible	32.100	1.22	39.162	109.800	1.4	153.720	133.000	1.4	186.200
Spine—Cervical vertebrae	13.400	1.22	16.348	32.907	1.4	46.070	54.541	1.4	76.357
Spine—Thoracic vertebrae	26.600	1.22	32.452	68.919	1.4	96.487	138.152	1.4	193.413
Spine—LV and sacrum	10.000	1.22	12.200	26.174	1.4	36.644	51.892	1.4	72.649
Pelvis	28.900	1.22	35.258	76.000	1.4	106.400	151.000	1.4	211.400
Clavicles	2.620	1.22	3.196	6.850	1.4	9.590	13.700	1.4	19.180
Scapulae	9.640	1.22	11.761	25.300	1.4	35.420	50.400	1.4	70.560
Rib cage	34.000	1.22	41.480	87.400	1.4	122.360	174.000	1.4	243.600
Arm bones	45.410	1.22	55.400	121.000	1.4	169.400	239.000	1.4	334.600
Leg bones	61.311	1.22	74.799	207.072	1.4	289.901	610.000	1.4	854.000
Total Volume/Mass:	340.901		412.288	993.623		1,366.772	1,985.359		2,750.833
Integumentary system									
Skin of the trunk	54.506	1.05	57.231	121.000	1.09	131.890	224.360	1.09	244.552
Skin of the head and neck	29.900	1.05	31.395	65.500	1.09	71.395	92.100	1.09	100.389
Skin of the legs	28.300	1.05	29.715	75.000	1.09	81.750	195.000	1.09	212.550
Skin of the breasts	0.094	1.05	0.099	0.356	1.09	0.388	0.640	1.09	0.698
Skin of the male genitalia	0.741	1.05	0.778	1.480	1.09	1.613	2.640	1.09	2.878
Total Volume/Mass:	113.541		119.218	263.336		287.036	514.740		561.067
Additional organs/tissues									
Adrenal glands	5.610	1.02	5.722	3.390	1.03	3.492	5.070	1.03	5.222
Brain	371.900	1.03	383.057	838.400	1.04	871.936	1,194.000	1.04	1,241.760
Breast tissue	0.103	0.99	0.102	0.704	0.94	0.662	1.450	0.94	1.363
Eyes	5.300	1.07	5.671	6.500	1.07	6.955	10.900	1.07	11.663
Rest of body—Head/neck	216.569	1.05	227.397	657.125	1.05	689.981	891.382	1.05	935.951
Rest of body—Trunk	1,416.523	1.02	1,444.853	3,738.139	1.03	3,850.283	7,499.189	1.03	7,724.165
Rest of body—Legs	389.689	1.05	409.173	1,262.928	1.05	1,326.074	3,770.000	1.05	3,958.500
Spleen	8.760	1.04	9.110	24.500	1.06	25.970	46.400	1.06	49.184
Thymus	10.800	1.02	11.016	26.425	1.03	27.218	28.500	1.03	29.355
Thyroid	1.200	1.05	1.260	1.700	1.05	1.785	3.300	1.05	3.465
Total Volume/Mass:	2,426.454		2,497.363	6,559.811		6,804.356	13,450.191		13,960.628
Hermaphrodite									
Total body mass (g):			3,523.125			9,737.727			19,587.568
Total body mass (kg):			3.52			9.74			19.59
Males (minus breast tissues)									
Total body mass (g):			3,523.023			9,737.066			19,586.205
Total body mass (kg):			3.52			9.74			19.59
Females (minus genitalia/testes)									
Total body mass (g):			3,517.535			9,725.241			19,563.656
Total body mass (kg):			3.52			9.73			19.56

mass (42% to 69%). This same organ mass (33.7 g in the revised 15-y-old phantom), however, is noted to be only 4% lower than the thymus mass assigned to the 15-y-old male in ICRP Publication 89. Again, no comparison is made to the new ICRP 89 reference 15-y-old female, as she was not defined at the time the original ORNL series was established. As was done in ORNL/TM-12907, however, mass scaling of specific absorbed fractions from the 15-y-old phantom can be performed to yield data unique to this new and younger reference female. As was the case with the original series, the ICRP 89 reference adult female may be represented by the revised 15-y-old phantom to a far greater extent than in the adult phantom.

Table 6. Organ and tissue masses in the revised ORNL anatomic models of the 10-y-old, 15-y-old, and adult.

Organ/tissue	10-y model			15-y model			Adult model		
	Volume (cm^3)	Density ($g\ cm^{-3}$)	Mass (g)	Volume (cm^3)	Density ($g\ cm^{-3}$)	Mass (g)	Volume (cm^3)	Density ($g\ cm^{-3}$)	Mass (g)
Respiratory system									
External nose	5.256	1.05	5.519	6.865	1.05	7.208	6.904	1.05	7.249
Nasal cavity (see UFR—Skeleton)									
Sphenoid sinuses	2.869	0.001205	0.003	3.031	0.001205	0.004	3.533	0.001205	0.004
Ethmoid sinuses	2.190	0.001205	0.003	2.317	0.001205	0.003	2.697	0.001205	0.003
Frontal sinuses	5.721	0.001205	0.007	6.043	0.001205	0.007	7.046	0.001205	0.008
Maxillary sinuses	20.566	0.001205	0.025	21.731	0.001205	0.026	25.329	0.001205	0.031
Oral cavity	239.692	1.03	246.883	232.221	1.03	239.188	252.269	1.03	259.837
Larynx—Lumen	2.398	0.001205	0.003	3.970	0.001205	0.005	7.775	0.001205	0.009
Larynx—Mucosa	0.936	1.10	1.030	1.350	1.10	1.485	2.141	1.10	2.355
Larynx—Residual wall	1.840	1.10	2.024	2.536	1.10	2.790	3.907	1.10	4.298
Pharynx—Lumen	17.463	0.001205	0.021	23.165	0.001205	0.028	49.763	0.001205	0.060
Pharynx—Mucosa	4.348	1.05	4.565	5.413	1.05	5.684	8.370	1.05	8.789
Pharynx—Residual wall	8.057	1.05	8.460	9.715	1.05	10.201	14.520	1.05	15.246
Trachea—Lumen	8.100	0.001205	0.010	12.799	0.001205	0.015	19.925	0.001205	0.024
Trachea—Mucosa	1.325	1.03	1.365	1.899	1.03	1.956	2.510	1.03	2.585
Trachea—Residual wall	6.200	1.03	6.386	8.675	1.03	8.935	11.240	1.03	11.577
Main bronchi—Lumen	7.271	0.001205	0.009	10.826	0.001205	0.013	13.530	0.001205	0.016
Main bronchi—Mucosa	1.565	1.03	1.612	2.403	1.03	2.475	3.012	1.03	3.102
Main bronchi—Residual wall	6.564	1.03	6.761	9.827	1.03	10.122	12.347	1.03	12.717
Lung—Left	709.000	0.352	249.568	1,020.000	0.352	359.040	1,560.000	0.352	549.120
Lung—Right	821.000	0.352	288.992	1,180.000	0.352	415.360	1,810.000	0.352	637.120
Total Volume/Mass:	1,872.361		823.244	2,564.786		1,064.544	3,816.818		1,514.152
Alimentary system									
Salivary glands—Parotid	25.000	1.03	25.750	38.462	1.03	39.616	48.077	1.03	49.519
Salivary glands—Sublingual	12.500	1.03	12.875	19.231	1.03	19.808	24.038	1.03	24.759
Salivary glands—Submandibular	4.808	1.03	4.952	7.692	1.03	7.923	9.615	1.03	9.903
Esophagus—Content	3.656	0.001205	0.004	7.065	0.001205	0.009	8.856	0.001205	0.011
Esophagus—Mucosa	2.786	1.03	2.870	5.247	1.03	5.404	6.911	1.03	7.118
Esophagus—Residual wall	15.914	1.03	16.391	26.484	1.03	27.279	37.789	1.03	38.923
Stomach—Content	128.000	1.03	131.840	187.000	1.03	192.610	250.000	1.03	257.500
Stomach—Mucosa	27.599	1.03	28.427	39.381	1.03	40.562	52.729	1.03	54.311
Stomach—Residual wall	54.201	1.03	55.827	73.619	1.03	75.828	99.271	1.03	102.249
Small intestine	447.000	1.03	460.410	806.000	1.03	830.180	1,060.000	1.03	1,091.800
Right colon—Content	67.300	1.03	69.319	121.400	1.03	125.042	159.800	1.03	164.594
Right colon—Mucosa	15.685	1.03	16.156	28.239	1.03	29.086	37.383	1.03	38.504
Right colon—Residual wall	48.615	1.03	50.073	87.412	1.03	90.034	114.319	1.03	117.749
Left colon—Content	58.420	1.03	60.173	106.930	1.03	110.138	139.230	1.03	143.407
Left colon—Mucosa	15.070	1.03	15.522	28.029	1.03	28.870	41.165	1.03	42.400
Left colon—Residual wall	47.220	1.03	48.637	84.612	1.03	87.150	105.645	1.03	108.814
Rectosigmoid colon—Content	41.367		21.549	73.994		38.653	102.780		56.008
Rectosigmoid colon—Mucosa	7.261	1.03	7.479	12.953	1.03	13.342	16.965	1.03	17.474
Rectosigmoid colon—Residual wall	21.842	1.03	22.497	39.232	1.03	40.409	50.812	1.03	52.336
Liver	853.000	1.05	895.650	1,350.000	1.05	1,417.500	1,830.000	1.05	1,921.500
Gall bladder—Contents	24.937	1.03	25.685	47.100	1.03	48.513	53.596	1.03	55.204
Gall bladder—Wall	4.332	1.03	4.462	7.616	1.03	7.844	10.096	1.03	10.399
Pancreas	52.129	1.04	54.214	98.929	1.04	102.886	117.264	1.04	121.955
Total Volume/Mass:	1,978.642		2,030.762	3,296.627		3,378.686	4,376.341		4,486.437
Circulatory system									
Heart—Contents	210.000	1.06	222.600	334.000	1.06	354.040	437.000	1.06	463.220
Heart—Wall	145.000	1.05	152.250	231.000	1.05	242.550	303.000	1.05	318.150
Total Volume/Mass:	355.000		374.850	565.000		596.590	740.000		781.370

Electron absorbed fractions

One unique feature of the present study is the systematic tabulation of electron-absorbed fractions within all organs of the revised ORNL series. Under the current MIRD schema, non-penetrating radiations (electrons, beta particles, alpha particles, etc.) are assumed to

Table 6.—*Continued.*

Organ/tissue	10-y model			15-y model			Adult model		
	Volume (cm^3)	Density ($g\ cm^{-3}$)	Mass (g)	Volume (cm^3)	Density ($g\ cm^{-3}$)	Mass (g)	Volume (cm^3)	Density ($g\ cm^{-3}$)	Mass (g)
Urogenital system									
Kidneys—Renal cortex	116.260	1.05	122.073	166.880	1.05	175.224	201.500	1.05	211.575
Kidneys—Renal medulla	43.020	1.05	45.171	61.980	1.05	65.079	74.120	1.05	77.826
Kidneys—Renal pelvis	7.040	1.05	7.392	10.160	1.05	10.668	12.340	1.05	12.957
Urinary bladder—Contents	98.600	1.04	102.544	154.000	1.04	160.160	203.000	1.04	211.120
Urinary bladder—Mucosa	3.666	1.04	3.813	5.336	1.04	5.549	7.333	1.04	7.626
Urinary bladder—Residual wall	18.634	1.04	19.379	29.164	1.04	30.331	38.367	1.04	39.902
Prostate gland	1.563	1.03	1.610	4.189	1.03	4.315	15.300	1.03	15.759
Testes	1.820	1.04	1.893	15.000	1.04	15.600	37.600	1.04	39.104
Genitalia (Male)	34.380	1.03	35.411	94.000	1.03	96.820	158.400	1.03	163.152
Ovaries	3.010	1.05	3.161	10.100	1.05	10.605	10.100	1.05	10.605
Uterus	4.000	1.02	4.080	76.000	1.02	77.520	76.000	1.02	77.520
Total Volume/Mass:	331.993		346.527	626.809		651.871	834.060		867.146
Skeletal system									
Cranium	250.200	1.4	350.280	284.500	1.4	398.300	364.600	1.4	510.440
Upper facial region (less sinuses)	194.854	1.22	237.722	213.078	1.22	259.955	226.890	1.22	276.806
Teeth	26.000	1.4	36.400	30.200	1.4	42.280	31.200	1.4	43.680
Mandible	139.400	1.4	195.160	144.800	1.4	202.720	170.500	1.4	238.700
Spine—Cervical vertebrae	83.571	1.4	116.999	130.626	1.4	182.876	165.562	1.4	231.787
Spine—Thoracic vertebrae	232.284	1.4	325.198	418.900	1.4	586.460	548.208	1.4	767.491
Spine—LV and sacrum	87.143	1.4	122.000	157.258	1.4	220.161	205.774	1.4	288.084
Pelvis	258.000	1.4	361.200	460.000	1.4	644.000	606.000	1.4	848.400
Clavicles	23.200	1.4	32.480	41.600	1.4	58.240	54.700	1.4	76.580
Scapulae	85.700	1.4	119.980	154.000	1.4	215.600	202.000	1.4	282.800
Rib cage	295.000	1.4	413.000	531.000	1.4	743.400	694.000	1.4	971.600
Arm bones	403.862	1.4	565.407	731.000	1.4	1,023.400	956.000	1.4	1,338.400
Leg bones	1,239.136	1.4	1,734.790	2,100.000	1.4	2,940.000	2,800.000	1.4	3,920.000
Total Volume/Mass:	3,318.350		4,610.616	5,396.962		7,517.393	7,025.434		9,794.767
Integumentary system									
Skin of the trunk	368.990	1.09	402.199	914.000	1.09	996.260	1,359.000	1.09	1,481.310
Skin of the head and neck	114.700	1.09	125.023	214.800	1.09	234.132	280.100	1.09	305.309
Skin of the legs	363.000	1.09	395.670	866.000	1.09	943.940	1,190.000	1.09	1,297.100
Skin of the breasts	1.010	1.09	1.101	44.000	1.09	47.960	51.000	1.09	55.590
Skin of the male genitalia	4.050	1.09	4.415	13.500	1.09	14.715	23.400	1.09	25.506
Total Volume/Mass:	851.750		928.408	2,052.300		2,237.007	2,903.500		3,164.815
Additional organs/tissues									
Adrenal glands	6.940	1.03	7.148	10.100	1.03	10.403	13.529	1.03	13.935
Brain	1,264.400	1.04	1,314.976	1,310.200	1.04	1,362.608	1,467.600	1.04	1,526.304
Breast tissue	2.500	0.94	2.350	471.842	0.94	443.531	473.086	0.94	444.701
Eyes	12.400	1.07	13.268	12.400	1.07	13.268	15.200	1.07	16.264
Rest of body—Head/neck	1,028.114	1.05	1,079.520	1,120.729	1.05	1,176.765	1,361.688	1.05	1,429.772
Rest of body—Trunk	12,982.720	1.03	13,372.202	24,297.269	1.03	25,026.187	31,430.380	1.03	32,373.291
Rest of body—Legs	7,690.864	1.05	8,075.407	13,300.000	1.05	13,965.000	18,000.000	1.05	18,900.000
Spleen	74.400	1.06	78.864	119.000	1.06	126.140	144.312	1.06	152.971
Thymus	38.043	1.03	39.184	32.725	1.03	33.707	24.731	1.03	25.473
Thyroid	7.600	1.05	1.980	11.900	1.05	12.495	19.900	1.05	20.895
Total Volume/Mass:	23,107.981		23,990.899	40,686.165		42,170.105	52,950.426		54,903.606
Hermaphrodite									
Total body mass (g):			33,105.306			57,616.195			75,512.294
Total body mass (kg):			33.11			57.62			75.51
Males (minus breast tissues)									
Total body mass (g):			33,102.956			57,172.664			75,067.593
Total body mass (kg):			33.10			57.17			75.07
Females (minus genitalia/testes)									
Total body mass (g):			33,068.002			57,503.775			75,310.038
Total body mass (kg):			33.07			57.50			75.31

deposit their entire energy in the source organ or tissue within which they are emitted. At energies below 100 keV, this assumption is generally valid even for the smallest organs of the newborn phantom. At electron energies exceeding 100 keV, proper accounting for electron/beta-particle energy loss is required.

Fig. 2a show values of the self-absorbed fraction for electron sources emitted within the thymus of the revised ORNL phantom series. These values may be compared to those of Fig. 2b determined by the method of Stabin and Siegel (2003) whereby values for unit-density spheres of equivalent mass are assigned. To apply the latter method,

Table 7. Comparison of organ masses for ICRP 89 reference individuals and the revised ORNL series (hermaphrodites–newborn, 1 y, 5 y, 10 y).

	Newborn					1 y					5 y					10 y				
	ICRP 89	ORNL model	% Diff	Revised model	% Diff	ICRP 89	ORNL model	% Diff	Revised model	% Diff	ICRP 89	ORNL model	% Diff	Revised model	% Diff	ICRP 89	ORNL model	% Diff	Revised model	% Diff
Respiratory system																				
Larynx—wall	1.3			0.6	−56%	4			0.8	−79%	7			1.5	−78%	12			3.1	−75%
Trachea—wall	0.5			0.8	55%	1.5			2.3	54%	2.5			4.2	69%	4.5			7.8	72%
Lungs—with blood	60	50.6	−16%	60.2	0%	150	143.0	−5%	170.4	14%	300	290.0	−3%	345.0	15%	500	453.0	−9%	546.9	9%
Lungs—tissue only	30					80					125					210				
Alimentary system																				
Salivary glands	6			5.9	−2%	24			23.8	−1%	34			33.7	−1%	44			43.6	−1%
Esophagus wall	2	2.1	6%	2.1	4%	5	5.8	16%	5.7	15%	10	11.5	15%	11.4	14%	18	19.4	8%	19.3	7%
Stomach—wall	7	6.4	−8%	6.4	−9%	20	21.8	9%	21.5	8%	50	49.1	−2%	48.6	−3%	85	85.1	0%	84.3	−1%
Stomach—contents	40	10.6	−74%	10.5	−74%	67	36.2	−46%	35.8	−47%	83	75.1	−10%	74.4	−10%	117	133.0	14%	131.8	13%
Small intestine—w + c	86	52.9	−38%	52.4	−39%	178	138.0	−22%	136.0	−24%	337	275.0	−18%	273.0	−19%	533	465.0	−13%	460.4	−14%
Colon—wall	17	18.5	9%	18.0	6%	50	48.4	−3%	47.0	−6%	120	96.6	−20%	94.6	−21%	210	163.4	−22%	160.4	−24%
Colon—contents	48	18.2	−62%	17.8	−63%	80	47.0	−41%	45.7	−43%	100	94.5	−6%	90.9	−9%	140	159.2	14%	151.0	8%
Liver	130	121.0	−7%	122.9	−5%	330	292.0	−12%	295.1	−11%	570	584.0	2%	590.1	4%	830	887.0	7%	895.7	8%
Gall bladder—w + c	3.3	2.5	−23%	2.9	−11%	9.4	5.7	−39%	8.6	−8%	17.6	23.4	33%	18.5	5%	30.4	45.8	51%	30.1	−1%
Pancreas	6	2.8	−53%	5.4	−10%	20	10.3	−49%	18.6	−7%	35	23.6	−33%	32.8	−6%	60	30.0	−50%	54.2	−10%
Circulatory system																				
Heart—wall	20	25.4	27%	25.4	27%	50	50.6	1%	51.1	2%	85	92.8	9%	93.8	10%	140	151.0	8%	152.3	9%
Heart—content	26	36.5	40%	37.6	44%	48	72.7	51%	74.1	54%	135	134.0	−1%	136.7	1%	230	219.0	−5%	222.6	−3%
Urogenital system																				
Kidneys—whole (2)	25	22.9	−8%	22.6	−10%	70	62.9	−10%	63.5	−9%	110	116.0	5%	116.7	6%	180	173.0	−4%	174.6	−3%
Urinary bladder—wall	4	2.9	−28%	3.6	−10%	9	7.7	−14%	7.7	−14%	16	14.5	−9%	14.6	−9%	25	23.2	−7%	23.2	−7%
Testes (2)	0.85	0.8	−1%	0.8	−3%	1.5	1.2	−19%	1.4	−9%	1.7	1.6	−4%	1.6	−4%	2	1.9	−6%	1.9	−5%
Prostate gland	0.8			0.8	4%	1.0			0.9	−7%	1.2			1.2	3%	1.6			1.6	1%
Ovaries (2)	0.3	0.3	9%	0.3	7%	0.8	0.7	−11%	0.7	−10%	2.0	1.7	−14%	1.7	−13%	3.5	3.1	−11%	3.2	−10%
Uterus	4.0	3.9	−4%	3.8	−6%	1.5	1.5	−3%	1.4	−5%	3	2.7	−10%	2.7	−12%	4	4.2	4%	4.1	2%
Skeletal system																				
Skeletal regions	370	351.0	−5%	412.3	11%	1,170	1,140.0	−3%	1,366.8	17%	2,430	2,710.0	12%	2,750.8	13%	4,500	4,630.0	3%	4,610.6	2%
Integumentary system																				
Skin	175	118.0	−33%	119.2	−32%	350	271.0	−23%	287.0	−18%	570	538.0	−6%	561.1	−2%	820	888.0	8%	928.4	13%
Additional organs																				
Adrenal glands (2)	6	5.8	−3%	5.7	−5%	4	3.5	−12%	3.5	−13%	5	5.3	5%	5.2	4%	7	7.2	3%	7.1	2%
Brain	380	352.0	−7%	383.1	1%	950	884.0	−7%	871.9	−8%	1,245	1,260.0	1%	1,241.8	−0.3%	1,310	1,410.0	8%	1,315.0	0.4%
Breast tissue																				
Eyes (2)	6			5.7	−5%	7			7.0	−1%	11			11.7	6%	12			13.3	11%
Rest of body	2,094	2,360.0	13%	2,081.4	−1%	6,382	6,400.0	0%	5,866.3	−8%	12,725	13,300.0	5%	12,618.6	−1%	22,050	23,100.0	5%	22,527.1	2%
Spleen	9.5	9.1	−4%	9.1	−4%	29	25.5	−12%	26.0	−10%	50	48.3	−3%	49.2	−2%	80.0	77.4	−3%	78.9	−1%
Thymus	13	11.3	−13%	11.0	−15%	30	22.9	−24%	27.2	−9%	30	29.6	−1%	29.4	−2%	38	31.4	−16%	39.2	4%
Thyroid	1.3	1.3	−1%	1.3	−3%	1.8	1.8	−1%	1.8	−1%	3.4	3.5	1%	3.5	2%	7.9	7.9	0%	8.0	1%
Total body (kg)	3.5	3.6	2.9%	3.52	0.7%	10	10	−2.8%	9.74	−2.6%	19	20	4.2%	19.59	3.1%	32.0	33.20	3.8%	33.11	3.5%

Table 8. Comparison of organ masses for ICRP 89 reference individuals and the revised ORNL series (15 y and adult males and females).

	15 y (male)					Adult (male)					Adult (female)				
	ICRP 89	ORNL model	% Diff	Revised model	% Diff	ICRP 89	ORNL model	% Diff	Revised model	% Diff	ICRP 89	ORNL model	% Diff	Revised model	% Diff
Respiratory system															
Larynx—wall	22			4.3	−81%	28			6.7	−76%	19			4.3	−78%
Trachea—wall	7.5			10.9	45%	10			14.2	42%	8			10.9	36%
Lungs—with blood	900	651.0	−28%	787.0	−13%	1,200	1,000.0	−17%	1,202.1	0%	950	651.0	−31%	787.0	−17%
Lungs—tissue only	330					500					420				
Alimentary system															
Salivary glands	68			67.3	−1%	85			84.2	−1%	70			67.3	−4%
Esophagus wall	30	35.5	18%	32.7	9%	40	46.5	16%	46.0	15%	35	35.5	1%	32.7	−7%
Stomach—wall	120	118.0	−2%	116.4	−3%	150	158.0	5%	156.6	4%	140	118.0	−16%	116.4	−17%
Stomach—contents	200	195.0	−3%	192.6	−4%	250	260.0	4%	257.5	3%	230	195.0	−15%	192.6	−16%
Small intestine—w + c	800	838.0	5%	830.2	4%	1,000	1,100.0	10%	1,091.8	9%	880	838.0	−5%	830.2	−6%
Colon—wall	300	295.0	−2%	288.9	−4%	370	387.0	5%	377.3	2%	360	295.0	−18%	288.9	−20%
Colon—contents	240	285.0	19%	273.8	14%	300	375.0	25%	364.0	21%	320	285.0	−11%	273.8	−14%
Liver	1,300	1,400.0	8%	1,417.5	9%	1,800	1,910.0	6%	1,921.5	7%	1,400	1,400.0	0%	1,417.5	1%
Gall bladder—w + c	53	58.3	11%	56.4	7%	68	66.2	−3%	65.6	−4%	56	58.3	4%	56.4	1%
Pancreas	110	64.9	−41%	102.9	−6%	140	94.3	−33%	122.0	−13%	120	64.9	−46%	102.9	−14%
Circulatory system															
Heart—wall	230	241.0	5%	242.6	5%	330	316.0	−4%	318.2	−4%	250	241.0	−4%	242.6	−3%
Heart—content	430	347.0	−19%	354.0	−18%	510	454.0	−11%	463.2	−9%	370	347.0	−6%	354.0	−4%
Urogenital system															
Kidneys—whole (2)	250	248.0	−1%	251.0	0%	310	299.0	−4%	302.4	−2%	275	248.0	−10%	251.0	−9%
Urinary bladder—wall	40	35.9	−10%	35.9	−10%	50	47.6	−5%	47.5	−5%	40	35.9	−10%	35.9	−10%
Testes (2)	16	15.5	−3%	15.6	−2%	35	39.1	12%	39.1	12%					
Prostate gland	4			4.3	0%	17			15.8	−7%					
Ovaries (2)											11	10.5	−5%	10.6	−4%
Uterus											80	79.0	−1%	77.5	−3%
Skeletal system															
Skeletal regions	7,950	7,650.0	−4%	7,517.4	−5%	10,500	10,000.0	−5%	9,794.8	−7%	7,800	7,650.0	−2%	7,517.4	−4%
Integumentary system															
Skin	2,000	2,150.0	8%	2,237.0	12%	3,300	3,010.0	−9%	3,164.8	−4%	2,300	2,150.0	−7%	2,237.0	−3%
Additional organs															
Adrenal glands (2)	10	10.5	5%	10.4	4%	14	16.3	16%	13.9	0%	13	10.5	−19%	10.4	−20%
Brain	1,420	1,410.0	−1%	1,362.6	−4%	1,450	1,420.0	−2%	1,526.3	5%	1,300	1,410.0	8%	1,362.6	5%
Breast tissue											500	351.0	−30%	443.5	−11%
Eyes (2)	13			13.3	2%	15			16.3	8%	15			13.3	
Rest of body	40,110	40,000.0	0%	40,168.0	0%	51,510	51,800.0	1%	52,703.1	2%	42,630	40,000.0	−6%	40,168.0	−6%
Spleen	130	123.0	−5%	126.1	−3%	150	183.0	22%	153.0	2%	130	123.0	−5%	126.1	−3%
Thymus	35	28.4	−19%	33.7	−4%	25	20.9	−16%	25.5	2%	20	28.4	42%	33.7	69%
Thyroid	12	12.4	3%	12.5	4%	20	20.7	4%	20.9	4%	17	12.4	−27%	12.5	−27%
Total body (kg)	56	56.8	1.4%	57.2	2.1%	73	73.7	1%	75.1	2.8%	60	56.8	−5.3%	57.2	−4.7%

the authors recommend energy- and mass-interpolation of the tabular data of Stabin and Konijnenberg (2000). A visual comparison of Figs. 2a and b shows that for the thymus excellent agreement between the two methods is noted up to 1 MeV. Above that energy, values given in Fig. 2a are slightly lower (i.e., greater escape of kinetic energy) than those in Fig. 2b. This level of agreement is expected in that the thymus is modeled within the phantom series as a single ellipsoid, and thus the only major difference in the two data sets is the assumption of organ shape, and to a lesser extent its tissue composition and density.

In Figs. 3 and 4, a similar comparison is made for the electron self-absorbed fraction within the thyroid and salivary glands, respectively [data of Fig. 3a are noted to be good agreement with values reported by Ulanovsky and Eckerman (1998)]. In both organs, the method of Stabin and Siegel (2003) is shown to underestimate the amount of electron energy escape in comparison to values given by direct radiation transport in the revised ORNL phantoms. Organ shape is a major factor in the discrepancy as the two thyroid lobes are explicitly modeled in the phantom series, and the salivary glands are modeled as six different glandular tissue regions. In both cases, the unit-density sphere approximation underestimates the organ's surface-to-volume ratio, and thus does not properly account for electron transport at the organ boundary. A similar problem would be expected for paired organs such as the breasts, ovaries, kidneys, and testes. The solution, of course, would be to treat each paired organ individually (e.g., left and right) as is proposed in the current study. Finally, it is interesting to note the slight concave change in shape of the newborn and 1-y phantom curves in Fig. 3a, where at energies above ~1.5 MeV electron energy loss from one lobe of the thyroid is partially absorbed in the neighboring lobe. This feature is, of course, absent in the data of Fig. 3b.

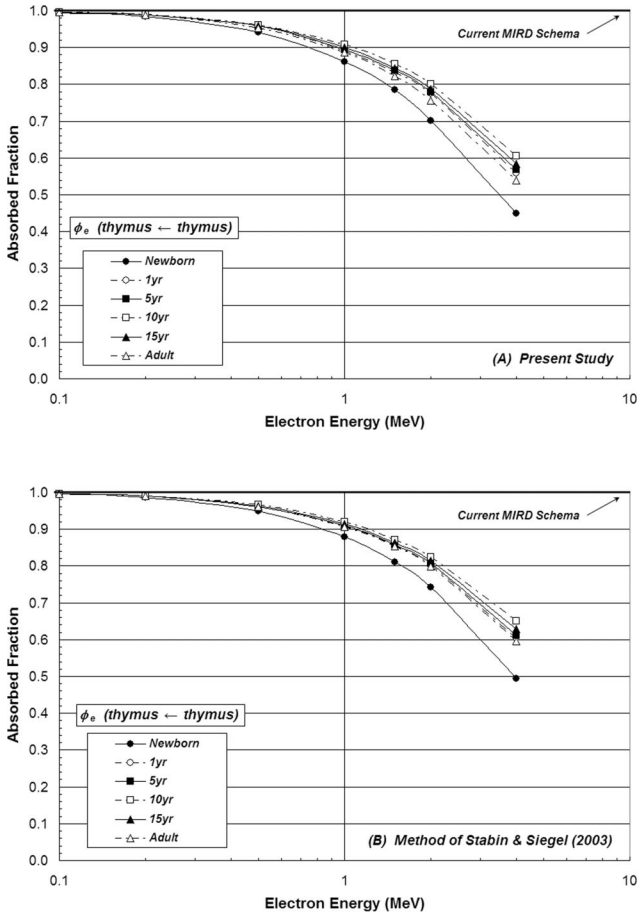

Fig. 2. Electron absorbed fractions of the self-irradiation of the thymus as a function of electron energy and subject age: (a) current study and (b) interpolation from the unity-density sphere data tables of Stabin and Konijnenberg (2000).

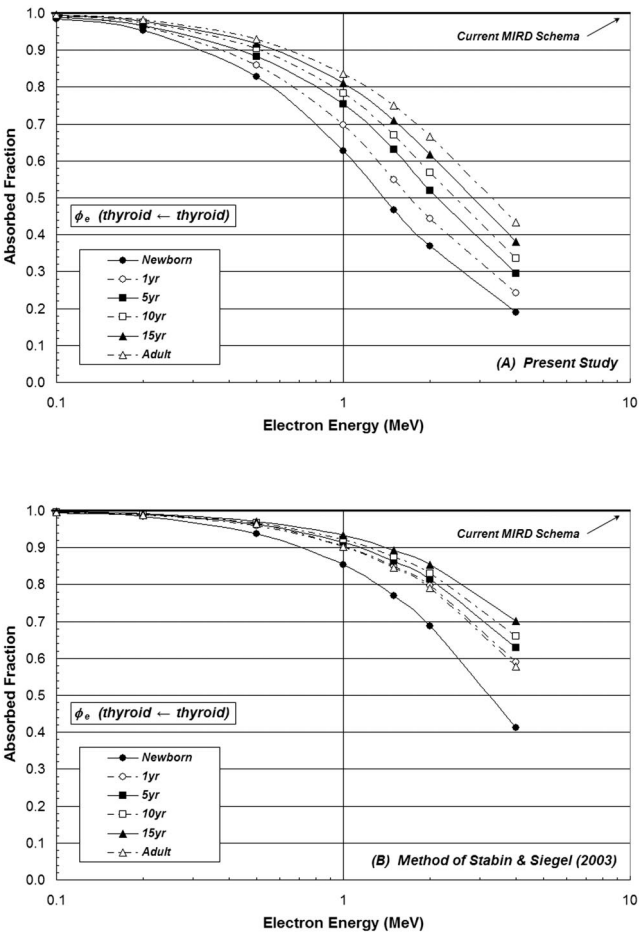

Fig. 3. Electron absorbed fractions of the self-irradiation of the thyroid gland as a function of electron energy and subject age: (a) current study and (b) interpolation from the unity-density sphere data tables of Stabin and Konijnenberg (2000).

Similarly, appreciable salivary gland electron crossfire is noted to occur only in the newborn phantom as shown Fig. 4b.

Fig. 5a demonstrates values of cross-organ absorbed fraction for electron sources in the right kidney of the adult phantom. Closed symbols denote a uniform source of electrons throughout the right kidney, while open symbols denote an electron source localized only within the right renal cortex. Target organs/tissues are the liver (circles) and the rest-of-body (squares). Essentially no change in electron energy deposition to the liver is noted between a whole-kidney electron source and one localized solely in the renal cortex. However, a slight increase in the absorbed fraction to the rest-of-body is noted for a right renal cortex source. When the electron source is localized within the right renal medulla as shown in Fig. 5b, a greater divergence is seen in values of ϕ(ROB ← kidney) and ϕ(ROB ← renal medulla) when compared to values given in Fig. 5a. Finally, Fig. 5c places the electron activity within the renal pelvis. Here, the energy lost to the rest-of-body increases to a value intermediate to that given by cortex and medulla sources, as only a small tissue layer separates the medial boundary of the MIRD 19 renal pelvis from the surrounding tissues of the phantom.

Stomach mucosa as both an electron source and target tissue

At present, the MIRD schema assigns the absorbed dose to the stomach (ST) wall for electron sources in the stomach contents via the following specific absorbed fractions:

$$\Phi(\text{ST wall} \leftarrow \text{ST cont}) = \frac{\Phi(\text{ST cont} \leftarrow \text{ST cont})}{2} = \frac{1}{2}\left(\frac{1}{m_{\text{ST cont}}}\right), \quad (7)$$

where $m_{\text{ST cont}}$ is the mass of the stomach contents. Noting that the specific absorbed fraction is given as the ratio of the absorbed fraction and the mass of the target tissue,

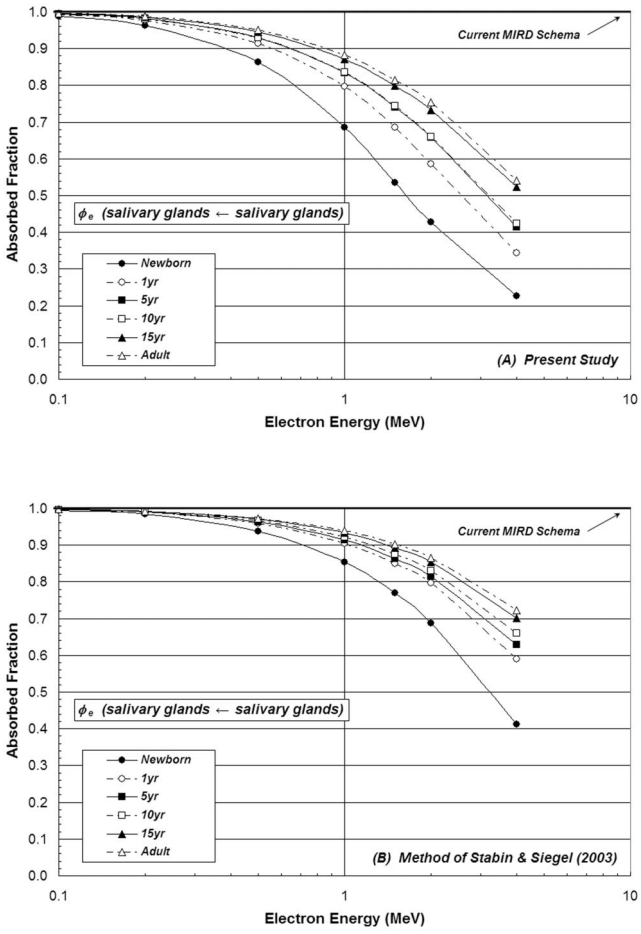

Fig. 4. Electron absorbed fractions of the self-irradiation of the salivary glands as a function of electron energy and subject age: (a) current study and (b) interpolation from the unity-density sphere data tables of Stabin and Konijnenberg (2000).

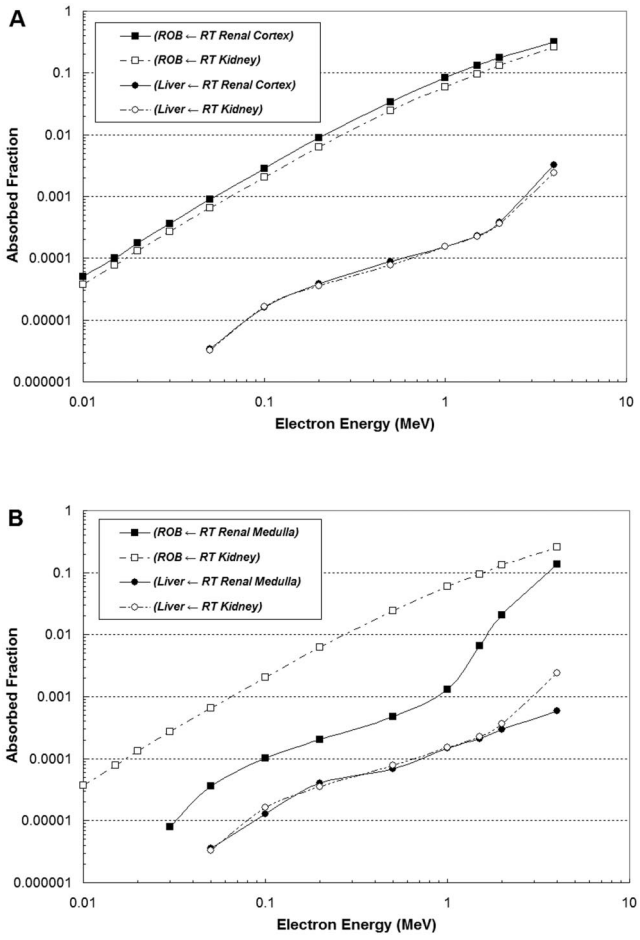

Fig. 5. Electron absorbed fractions to rest-of-body and the liver for electron sources localized in (a) the right renal cortex, (b) the right renal medulla, or (c) the right renal pelvis of the adult. Open symbols represent electron transport for uniform source within the right kidney.

one can estimate an effective absorbed fraction from eqn (7) using the wall and content masses of the stomach in the adult ORNL model:

$$\phi(\text{ST wall} \leftarrow \text{ST cont})_{\text{eff}} = \frac{1}{2}\left(\frac{m_{\text{ST wall}}}{m_{\text{ST cont}}}\right) \approx 0.304. \quad (8)$$

In the present study, however, the stomach mucosa is defined as the target layer of interest for both electron and photon emissions in the stomach contents; consequently, a slightly revised effective absorbed fraction would be given under the MIRD schema for stomach mucosa:

$$\phi(\text{ST mucosa} \leftarrow \text{ST cont})_{\text{eff}} = \frac{1}{2}\left(\frac{m_{\text{ST mucosa}}}{m_{\text{ST cont}}}\right) \approx 0.105. \quad (9)$$

Both these energy-independent values of effective absorbed fraction are shown in Fig. 6, along with the results of electron transport simulation using the revised ORNL adult stomach model with the stomach mucosa defined as the target tissue. As shown, the traditional MIRD schema significantly overestimates the true electron energy deposited within the mucosa layer at electron energies below 1 MeV. At electron energies exceeding 1 MeV, the MCNP-derived value of $\phi(\text{ST mucosa} \leftarrow \text{ST cont})_{\text{eff}}$ is shown to approach a constant value of 0.05, a value lower that given under eqn (9) by a factor of ~2 and lower that that given by eqn (8) by a factor of ~6. These results are consistent with studies of electron depth-dose in the alimentary tract organs by Poston et al. (1996) and Stubbs et al. (1998).

Recent studies in the nuclear medicine literature indicate radiopharmaceutical localization may occur within the walls of the alimentary tract organs, particularly within their mucosal layers (Fisher et al. 2004). In Fig. 7, we show values of electron absorbed fraction for

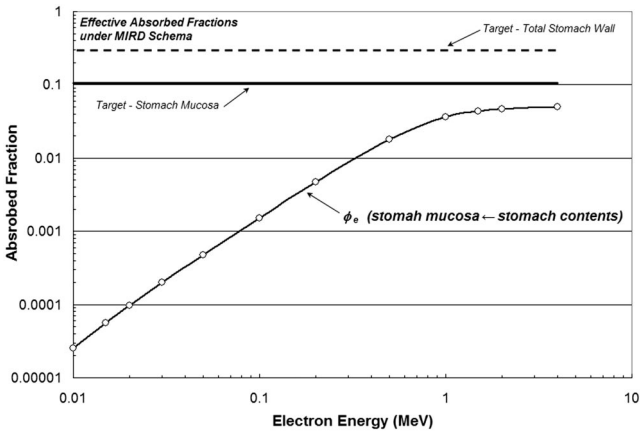

Fig. 6. Electron absorbed fractions to the stomach mucosa from sources localized in the stomach contents (adult model). Approximate values for the surface dose given by the MIRD schema are indicated by horizontal lines (solid—stomach mucosa target, and dashed—total stomach wall).

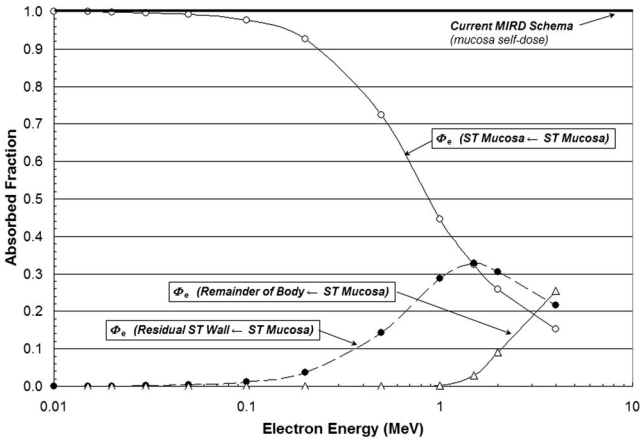

Fig. 7. Electron absorbed fractions to the stomach mucosa, residual wall, and surrounding tissues (rest-of-body) for sources localized in the stomach mucosa.

an electron source localized in the stomach mucosa of the revised adult phantom. Three target tissues are considered: the stomach mucosa itself (open circles), the residual tissues of the stomach wall (solid circles), and the rest-of-body tissues surrounding the organ (open triangles). Under the traditional MIRD schema, full energy deposition would be assigned to the source tissue at all electron energies. Fig. 7 indicates that at electron energies exceeding 100 keV, an increasing fraction of electron emission energy is delivered to the residual tissues of the stomach wall (submucosa, muscularis externa, and serosa), which peaks at ~32% at 1.5 MeV. At energies exceeding ~1 MeV, electrons emitted within the stomach mucosa begin to penetrate the stomach wall altogether and thus, at 4 MeV, ~25% of the total electron emission energy is deposited outside the organ.

Radionuclide *S* values for ^{131}I and ^{90}Y

To understand the clinical significance of electron transport, radionuclide *S* values were calculated for self-irradiation of the following organs by ^{131}I and ^{90}Y at all phantom ages: left ovary, thyroid, spleen, left lung, and liver. Both radionuclides are in current use in radionuclide cancer therapy for non-Hodgkin's lymphoma (Larson and Krenning 2005). The results are given in Table 9 in the form of *S* value ratios where the numerator is the *S* value without electron transport ($\phi = 1$ for electrons and beta particles) and the denominator is that with explicit consideration of electron transport ($\phi < 1$). Ratios greater than unity thus indicate the degree to which existing MIRD schema estimates of organ self-dose are potentially overestimated for a given reference organ in the phantom series. Higher *S* value ratios are expected for ^{90}Y where the mean beta-particle energy per decay is 934.6 keV. The mean energy per decay for ^{131}I is 191.7 keV for electron/beta emissions and 381.6 keV for photon emissions.

For ^{131}I, *S* values calculated under the current MIRD schema (with no electron transport) are shown to be conservative by no more than 5% for all organs considered in the adult and 15-y phantoms. *S* value ratios exceed 1.05 for the ovaries only in the 5-y and 10-y phantoms, and for both the thyroid and ovaries in the newborn and 1-y phantoms. It is of interest to note that electron transport appears to be more important in the left lung than in the spleen of the smallest two phantoms, even through the total mass of the left lung exceeds that

Table 9. Ratio of the radionuclide *S* value calculated without consideration of electron or beta-particle transport to that with consideration of electron or beta-particle transport.

	S value ratio for ^{131}I						*S* value ratio for ^{90}Y					
Organ	Newborn	1-y-old	5-y-old	10-y-old	15-y-old	Adult	Newborn	1-y-old	5-y-old	10-y-old	15-y-old	Adult
Left ovary	1.13	1.09	1.07	1.06	1.04	1.04	2.23	1.87	1.62	1.50	1.30	1.30
Thyroid	1.10	1.07	1.05	1.05	1.04	1.04	1.80	1.59	1.42	1.40	1.34	1.43
Spleen	1.03	1.02	1.02	1.01	1.01	1.01	1.21	1.14	1.12	1.10	1.09	1.09
Left lung	1.06	1.04	1.03	1.02	1.02	1.02	1.44	1.28	1.21	1.18	1.16	1.14
Liver	1.01	1.01	1.01	1.01	1.01	1.01	1.10	1.08	1.06	1.05	1.05	1.04
UB mucosa	1.63	1.75	1.88	1.94	1.88	1.97	1.23	1.20	1.25	1.25	1.17	1.23

of the spleen. The greater electron escape is accounted for by the substantially lower mass density assigned to the lungs.

Transport of ^{90}Y beta particles is significantly more important across all organs and all phantom ages. Minimal errors in dosimetry (defined arbitrarily as *S* value ratios $\leq$1.05) are only seen for the liver at a phantom age of 10 y and older. Even in the adult, the current MIRD schema is shown to overestimate the self-dose to the ovaries by 30% and the thyroid by 43%, the latter being somewhat higher owing to its increased surface-to-volume ratios as compared to the ovaries. For the lungs in the adult, a 14% overestimate in ^{90}Y self-dose is further noted. At the very youngest ages, the degree of overestimation in the ^{90}Y self-dose is found to range from 50% to greater than a factor of 2. The clinical relevance of these calculations, however, becomes less at the younger ages where radionuclide therapies using ^{90}Y are increasingly less common.

At the bottom of Table 9 are ratios of ϕ(urinary bladder mucosa ← urinary bladder content) under the current MIRD schema (electron dose at wall surface and photon dose averaged across the entire wall) to that calculated under the methods discussed above (explicit consideration of both electron and photon transport across a defined mucosal layer). The current MIRD schema is shown to overestimate the absorbed dose to the mucosal layer by factors of 1.63 to 1.97 for the lower-energy electron/beta emissions from ^{131}I. The overestimate in mucosal layer dose is noted to be less for ^{90}Y (factors ranging from 1.17 to 1.23).

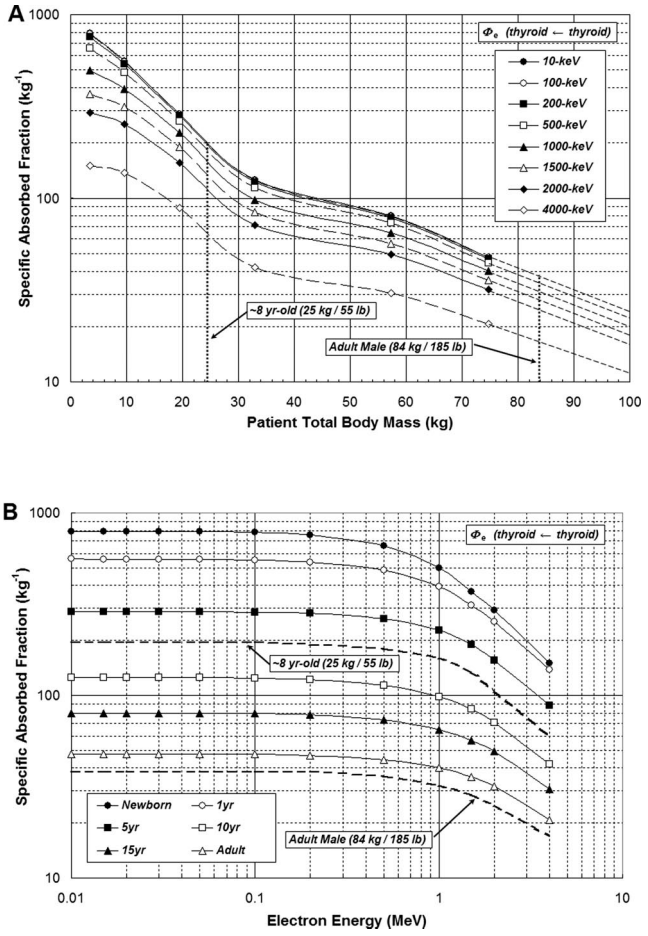

Fig. 8. Electron specific absorbed fractions for self-dose to the thyroid as (a) function of patient total body mass, and (b) function of electron energy. Dashed lines indicate values obtained by either interpolation or extrapolation.

Estimates of patient-specific values of electron and photon values of *F*

In 1989, the ICRP introduced the concept of age-dependent doses to members of the general public in which specific absorbed fractions for organ cross-dose and self-dose (as well as corresponding *SEE* and *S* values) were permitted to vary in a continuous manner with subject age (or age post-intake) from their discrete values in the ORNL phantom series (ICRP 1989). In a very similar manner, values of organ self-dose and cross-dose for both internally emitted electrons and photons from the revised ORNL series can be used to provide approximations of their patient-specific values through interpolation or extrapolation. In Fig. 8a, energy-dependent values of electron specific absorbed fraction for thyroid self-dose are plotted as a function phantom total body mass (TBM) in kg. Consider for the moment that values of Φ(thyroid ← thyroid)$_{electron}$ are sought for two patients—an 8-y-old with a TBM of 25 kg, and an adult with a TBM of 84 kg. For the pediatric patient, energy-dependent values of Φ(thyroid ← thyroid)$_{electron}$ are obtained via interpolation between values for the 5-y model (19.6 kg) and the 10-y model (33.1 kg), while values for the adult patient are taken from semi-log extrapolations from data obtained with the 75-kg adult model. These interpolated and extrapolated values of Φ(thyroid ← thyroid)$_{electron}$ are then plotted in Fig. 8b along with their neighboring phantom's values.

This concept of patient-specific scaling of the specific absorbed fraction is further extended to photon cross-organ dose in Figs. 9a and b. In Fig. 9a, values of Φ(thyroid ← right lung)$_{photon}$ are plotted as a function of phantom TBM. Again, interpolated values are taken as representative of a pediatric patient at 25 kg, and a slightly larger adult patient at 84 kg. These values of photon specific absorbed fraction are then re-plotted as a function of photon energy in Fig. 9b, where dashed lines indicate their approximation to patient-specific values. For a given radionuclide, patient-specific values of Φ(thyroid ← right lung)$_{photon}$ can be selected across the

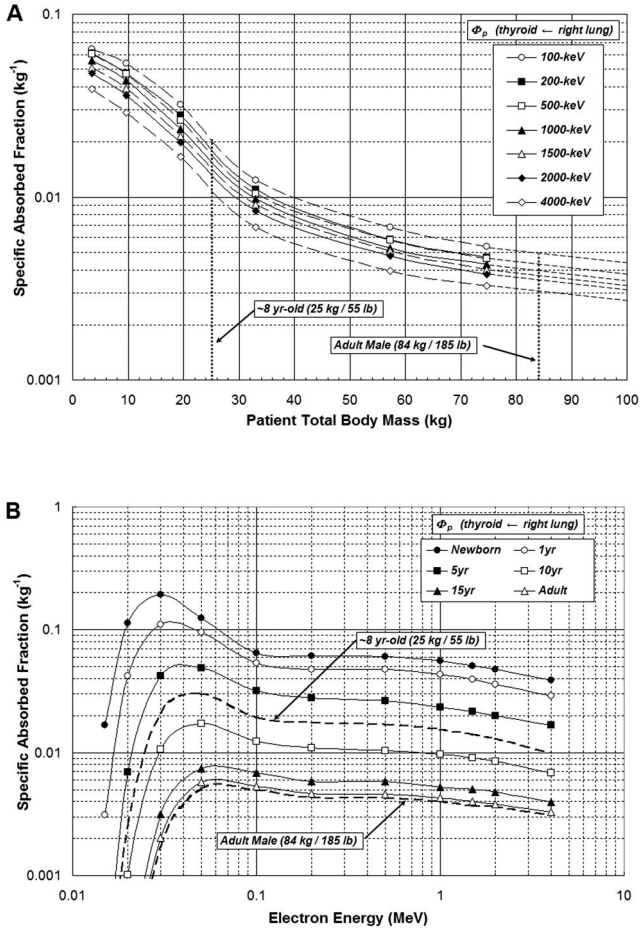

Fig. 9. Photon specific absorbed fractions to the thyroid for photon sources localized in the right lung. Values of Φ are given for (a) function of patient total body mass, and (b) function of photon energy. Dashed lines indicate values obtained by either interpolation or extrapolation.

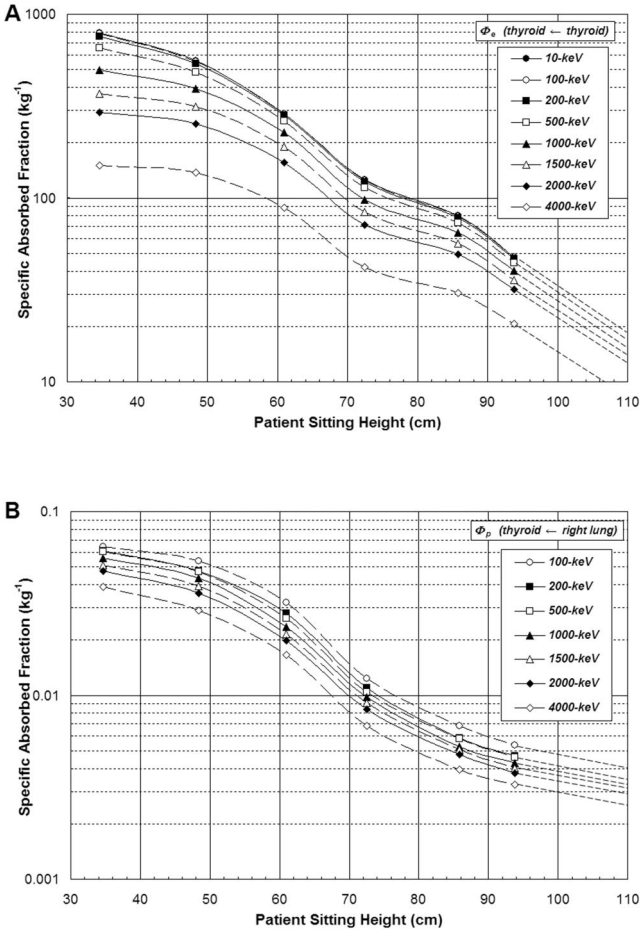

Fig. 10. Values of specific absorbed fraction as a function of patient sitting height: (a) $\Phi(\text{thyroid} \leftarrow \text{thyroid})_{\text{electron}}$ and (b) $\Phi(\text{thyroid} \leftarrow \text{right lung})_{\text{photon.}}$

photon energy spectrum in the determination of a patient-specific radionuclide *S* value.

For pediatric patients, it can be argued that patient-specific values of Φ_{photon} or Φ_{electron} can be reasonably obtained through interpolation across the ORNL phantom series using total body mass as the dependent variable. For adult patients, however, increasing total body mass can, in many cases, be the result of increasing subcutaneous fat and thus changes in TBM may not reflect corresponding changes in Φ_{photon}. An alternate method would then be to interpolate (or extrapolate) phantom-specific values of the Φ using sitting height as the dependent variable. Sitting height has been suggested to be a more appropriate indicator of inter-organ separation distances (Huh and Bolch 2003). This approach is demonstrated in Fig. 10a for values of $\Phi(\text{thyroid} \leftarrow \text{thyroid})_{\text{electron}}$ and in Fig. 10b for values of $\Phi(\text{thyroid} \leftarrow \text{right lung})_{\text{photon}}$.

Obviously, when detailed anatomical models of individual patients are available through regional CT or MR scans, Monte Carlo radiation transport simulations using corresponding segmented patient anatomy will provide the most accurate estimates of patient-specific internal photon and electron dose. The use of phantom-interpolated or phantom-extrapolated values of Φ, however, represents a consistent method for obtaining these values when whole-body imaging data are not available. Furthermore, they represent an improvement over simply assigning fixed ORNL phantom values to individual patients (e.g., applying values of Φ from either the 5-y phantom or the 10-y phantom to represent patient-specific values of Φ for an 8-y-old child).

CONCLUSION

In this paper, modifications to the ORNL series of stylized computational phantoms are described. These

revisions were made to (1) incorporate recent developments in stylized models of the head, brain, kidneys, rectosigmoid colon, and extra-pulmonary airways, (2) incorporate new models of the salivary glands and the mucosa layer of the urinary bladder, alimentary tract organs, and respiratory airways, (3) adopt reference values of elemental tissue compositions and mass densities from ICRP Publication 89 and ICRU Report 46, (4) provide for explicit treatment of left and right organs within organ pairs, (5) provide for a systematic tabulation of electron absorbed fractions as a function of energy and subject age, and (6) provide for methods of reporting patient-specific values of the specific absorbed fraction for both electrons and photons through interpolation/extrapolation of their phantom-derived values. While tomographic computational phantoms provide improved anatomic realism, there does not yet exist a comprehensive series of pediatric models, nor the ability to simulate very fine anatomic structures as can be modeled via mathematical approximation. Consequently, stylized pediatric phantoms will continue to fill a data need in medical radiation dosimetry.

Acknowledgments—This work was supported by grant R32/CCR416743 from the Centers for Disease Control and Prevention (CDC) with the University of Florida. Its contents are solely the responsibility of the authors and do not necessarily represent the official views of the CDC.

REFERENCES

Bergman RA, Afifi AK, Heidger PM. Atlas of microscopic anatomy: a functional approach: companion to histology and neuroanatomy. Philadelphia: Saunders; 1989.

Berman I. Color atlas of basic histology. New York and London: McGraw-Hill; 2003.

Bolch W, Pomije B, Sessions J, Arreola M, Williams J. A video analysis technique for organ dose assessment in pediatric fluoroscopy: applications to voiding cystourethrograms (VCUG). Med Phys 30:667–680; 2003.

Bouchet LG, Bolch WE, Weber DA, Atkins HL, Poston JW, Sr. MIRD Pamphlet No. 15: Radionuclide S values in a revised dosimetric model of the adult head and brain. Medical internal radiation dose. J Nucl Med 40:62S–101S; 1999a.

Bouchet LG, Bolch WE, Wessels BA, Weber DA. Head and brain dosimetry: absorbed fractions of energy and absorbed dose per unit cumulated activity within pediatric and adult head and brain models for use in nuclear medicine internal dosimetry. Reston, VA: The Society of Nuclear Medicine; 1999b.

Bouchet L, Bolch W, Blanco P, Wessels B, Siegel J, Rajon D, Clairand I, Sgouros G. MIRD Pamphlet No. 19: Absorbed fractions and radionuclide S values for six age-dependent multi-region models of the kidney. J Nucl Med 44:1113–1147; 2003.

Briesmeister JF. MCNP—A general Monte Carlo N-particle transport code. Los Alamos, NM: Los Alamos National Laboratory; LA-12625-M; 1997.

Burkitt HG, Young B, Heath JW, Wheater PR. Wheater's functional histology: a text and colour atlas. Edinburgh and New York: Churchill Livingstone; 1993.

Caon M, Bibbo G, Pattison J. An EGS4-ready tomographic computational model of a 14-year-old female torso for calculating organ doses from CT examinations. Phys Med Biol 44:2213–2225; 1999.

Chibani O, Li XA. Monte Carlo dose calculations in homogeneous media and at interfaces: a comparison between GEPTS, EGSnrc, MCNP, and measurements. Med Phys 29:835–847; 2002.

Cristy M. Mathematical phantoms representing children of various ages for use in estimates of internal dose. Oak Ridge, TN: Oak Ridge National Laboratory; ORNL/NUREG/TM-367; 1980.

di Fiore MSH, Eroschenko VP. Atlas of normal histology. Philadelphia: Lea & Febiger; 1989.

di Fiore MSH, Schmidt IG. Atlas of human histology. Philadelphia: Lea & Febiger; 1981.

Eckerman KF, Ryman JC. External exposure to radionuclides in air, water, and soil. Washington, DC: U.S. Environmental Protection Agency; Federal Guidance Report No. 12; 1993.

Eckerman K, Leggett R, Nelson C, Puskin J, Richardson A. Cancer risk coefficients for environmental exposures to radionuclides. Washington, DC: U.S. Environmental Protection Agency; Federal Guidance Report No. 13; 1999.

Eroschenko VP, di Fiore MSH. Atlas of histology with functional correlations. Philadelphia: Lippincott Williams & Wilkins; 2000.

Farfán E, Han E, Huh C, Huston T, Bolch E, Bolch W. A revised stylized model of the extrathoracic and thoracic airways for use with the ICRP-66 respiratory tract model. Health Phys 86:337–352; 2004.

Fisher D, Rajon D, Breitz H, Goris M, Bolch W, Knox S. Dosimetry model for radioactivity localized to intestinal mucosa. Cancer Biother Radiopharm 19:293–307; 2004.

Gartner LP, Hiatt JL. Atlas of histology. Baltimore: Williams & Wilkins; 1987.

Herrath E. Atlas of histology: normal microscopic anatomy of man. New York: Hafner Co.; 1966.

Howell RW. The MIRD schema: from organ to cellular dimensions. J Nucl Med 35:531–533; 1994.

Huh C, Bolch WE. A review of US anthropometric reference data (1971–2000) with comparisons to both stylized and tomographic anatomic models. Phys Med Biol 48:3411–3429; 2003.

Huh C, Bhutani M, Farfan E, Bolch W. Individual variations in mucosa and total wall thickness in the stomach and rectum assessed via endoscopic ultrasound. Physiol Meas 24:N15–N22; 2003.

ICRU. Photon, electron, proton and neutron interaction data for body tissues. Bethesda, MD: International Commission on Radiation Units and Measurements; ICRU Report 46; 1992.

ICRP. Report on the Task Group on Reference Man. Oxford, UK: International Commission on Radiological Protection; ICRP Publication 23:62–98; 1975.

ICRP. Age-dependent doses to members of the public from intake of radionuclides: Part 1. Elmsford, NY: International Commission on Radiological Protection; ICRP Publication 56; 1989.

ICRP. Age-dependent doses to members of the public from intake of radionuclides: Part 2—ingestion dose coefficients. Elmsford, NY: International Commission on Radiological Protection; ICRP Publication 67; 1993.

ICRP. Dose coefficients for intakes of radionuclides by workers (replacement for ICRP Publication 61). Oxford, UK:

International Commission on Radiological Protection; ICRP Publication 68; 1994.

ICRP. Age-dependent doses to members of the public from intake of radionuclides: Part 3—ingestion dose coefficients. Elmsford, NY: International Commission on Radiological Protection; ICRP Publication 69; 1995a.

ICRP. Age-dependent doses to members of the public from intake of radionuclides: Part 4—inhalation dose coefficients. Elmsford, NY: International Commission on Radiological Protection; ICRP Publication 71; 1995b.

ICRP. Doses to the embryo and fetus from intakes of radionuclides by the mother. Elmsford, NY: International Commission on Radiological Protection; ICRP Publication 88; 2001.

ICRP. Basic anatomical and physiological data for use in radiological protection: reference values. New York: International Commission on Radiological Protection; ICRP Publication 89; 2002.

Jones DG, Wall BF. Organ doses from medical x-ray examinations calculated using Monte Carlo techniques. Chilton: National Radiological Protection Board; NRPB Report R186; 1985.

Junqueira LCU, Carneiro J. Basic histology. New York and London: McGraw-Hill; 2003.

Kerr JB. Atlas of functional histology. London and St. Louis: Mosby; 1999.

Larson SM, Krenning EP. A pragmatic perspective on molecular targeted radionuclide therapy. J Nucl Med 46(Suppl 1):1S–3S; 2005.

Mardirossian G, Tagesson M, Blanco P, Bouchet LG, Stabin M, Yoriyaz H, Baza S, Ljungberg M, Strand SE, Brill AB. A new rectal model for dosimetry applications. J Nucl Med 40:1524–1531; 1999.

Marieb EN. Human anatomy and physiology. Menlo Park, CA: Benjamin-Cummings Science Publishing; 2001.

Netter FH, Hansen JT. Atlas of human anatomy. Teterboro, NJ: Icon Learning Systems; 2003.

Nipper J, Williams J, Bolch W. Creation of two tomographic voxel models of pediatric patients in the first year of life. Phys Med Biol 47:3143–3164; 2002.

Poston JW Jr, Kodimer KA, Bolch WE, Poston JW, Sr. A revised model for the calculation of absorbed energy in the gastrointestinal tract. Health Phys 71:307–314; 1996.

Reith EJ, Ross MH. Atlas of descriptive histology. New York: Hoeber Medical Division Harper & Row; 1965.

Rosenstein M. Handbook of selected tissue doses for projections common in diagnostic radiology. Rockville, MD: Food and Drug Administration; FDA Report 89-8031; 1988.

Ross MH, Romrell LJ, Kaye GI. Histology: a text and atlas. 3rd edition. Baltimore: Williams & Wilkins; 1995.

Ross MH, Romrell LJ, Kaye GI. Histology: a text and atlas. 4th edition. Baltimore: Williams & Wilkins; 2002.

Sleisenger MH, Fordtran JS, Feldman M, Scharschmidt B. Sleisenger & Fordtran's gastrointestinal and liver disease: pathophysiology, diagnosis, management. Philadelphia: Saunders; 1998.

Stabin MG. MIRDOSE. Personal computer software for internal dose assessment in nuclear medicine. J Nucl Med 37:538–546; 1996.

Stabin MG, Konijnenberg MW. Re-evaluation of absorbed fractions for photons and electrons in spheres of various sizes. J Nucl Med 41:149–160; 2000.

Stabin MG, Siegel JA. Physical models and dose factors for use in internal dose assessment. Health Phys 85:294–310; 2003.

Stabin M, Sparks R. OLINDA—PC-based software for biokinetic analysis and internal dose calculations in nuclear medicine [Abstract]. J Nucl Med 44:103P; 2003.

Stabin M, Watson E, Cristy M, Ryman J, Eckerman K, Davis J, Marshall D, Gehlen M. Mathematical models and specific absorbed fractions of photon energy in the nonpregnant adult female and at the end of each trimester of pregnancy. Oak Ridge, TN: Oak Ridge National Laboratory; ORNL/TM-12907; 1995.

Staton R, Pazik F, Nipper J, Williams J, Bolch W. A comparison of newborn stylized and tomographic models for dose assessment in pediatric radiology. Phys Med Biol 48:805–820; 2003.

Stern SH, Rosenstein M, Renaud L, Zankl M. Handbook of selected tissue doses for fluoroscopic and cineangiographic examination of the coronary arteries. Rockville, MD: Food and Drug Administration; FDA Report 95-8288; 1995.

Stubbs J, Evans J, Stabin M. Radiation absorbed doses to the walls of hollow organs. J Nucl Med 39:1989–1995; 1998.

Suleiman OH, Anderson J, Jones B, Rao GU, Rosenstein M. Tissue doses in the upper gastrointestinal fluoroscopy examination. Radiol 178:653–658; 1991.

Tortora GJ, Anagnostakos NP. Principles of anatomy and physiology. New York: Harper & Row; 1984.

Ulanovsky A, Eckerman K. Absorbed fractions for electrons and photon emissions in the developing thyroid: fetus to the five-year-old. Radiat Prot Dosim 79:419–424; 1998.

Weiss L. Modern concepts of gastrointestinal histology. New York: Elsevier; 1984.

Zankl M, Veit R, Williams G, Schneider K, Fendel H, Petoussi N, Drexler G. The construction of computer tomographic phantoms and their application in radiology and radiation protection. Radiat Env Biophys 27:153–164; 1988.

Zhang S-X. An atlas of histology. New York: Springer; 1999.